Remote Sensing of Environment 233 (2019) 111345

Contents lists available at ScienceDirect

Remote Sensing of Environment

journal homepage: www.elsevier.com/locate/rse

Burned area detection and mapping using Sentinel-1 backscatter coefficient and thermal anomalies

Miguel A. Belenguer-Plomer[a,*], Mihai A. Tanase[a,b], Angel Fernandez-Carrillo[a], Emilio Chuvieco[a]

[a] Environmental Remote Sensing Research Group, Dep. of Geology, Geography and Environment, Universidad de Alcalá, Colegios 2, Alcalá de Henares 28801, Spain
[b] School of Ecosystem and Forest Sciences, University of Melbourne, Parkville 3052, Australia

ARTICLE INFO

Edited by Jing M. Chen

Keywords:
Burned area detection
Sentinel-1
Backscatter coefficient
SAR
Random forests
Reed-Xiaoli detector
Fire

ABSTRACT

This paper presents a burned area mapping algorithm based on change detection of Sentinel-1 backscatter data guided by thermal anomalies. The algorithm self-adapts to the local scattering conditions and it is robust to variations of input data availability. The algorithm applies the Reed-Xiaoli detector (RXD) to distinguish anomalous changes of the backscatter coefficient. Such changes are linked to fire events, which are derived from thermal anomalies (hotspots) acquired during the detection period by the Moderate Resolution Imaging Spectroradiometer (MODIS) and the Visible Infrared Imaging Radiometer Suite (VIIRS) sensors. Land cover maps were used to account for changing backscatter behaviour as the RXD is class dependent. A machine learning classifier (random forests) was used to detect burned areas where hotspots were not available. Burned area perimeters derived from optical images (Landsat-8 and Sentinel-2) were used to validate the algorithm results. The validation dataset covers 21 million hectares in 18 locations that represent the main biomes affected by fires, from boreal forests to tropical and sub-tropical forests and savannas. A mean Dice coefficient (DC) over all studied locations of 0.59 ± 0.06 (± confidence interval, 95%) was obtained. Mean omission (OE) and commission errors (CE) were 0.43 ± 0.08 and 0.37 ± 0.06, respectively. Comparing results with the MODIS based MCD64A1 Version 6, our detections are quite promising, improving on average DC by 0.13 and reducing OE and CE by 0.12 and 0.06, respectively.

1. Introduction

Fire is one of the natural agents that most alter terrestrial ecosystems and has a key ecological role in a large part of the Earth's surface. Fires may have local to global effects as they reduce soil fertility, change water supply, increase biodiversity loss and negatively influence carbon sequestration (Hoffmann et al., 2002; Van der Werf et al., 2010; Hansen et al., 2013; Bond et al., 2005; Aponte et al., 2016; Pausas & Paula, 2012; Lavorel et al., 2007). Fires may also alter global biochemical cycles by modifying the emitted greenhouse gases (GHGs) and aerosols presence in the atmosphere (Van Der Werf et al., 2017; Andreae & Merlet, 2001; Bowman et al., 2009). Annual global estimates of carbon emissions from forest fires are quite variable. Van der Werf et al. (2010) place them between 1.6 and 2.8 PgC per year, which is equivalent to 20 to 30% of the global carbon emissions generated by burning fossil fuels (Kloster et al., 2012; Flannigan et al., 2009). However, other authors estimate fire related emissions at 2 to 4 PgC per year, the equivalent of up to 50% of fossil fuel emissions (Bowman et al., 2009). Regardless of the actual value, changes in global burned area (BA) remains an important source of interannual variability of atmospheric carbon concentration. Direct relationships between global warming and the frequency of fires at the global level imply a positive feedback process with sufficient potential to be a key factor in climate change (Flannigan et al., 2009; Hoffmann et al., 2002; Knorr et al., 2016). Although the current understanding of all these interactions is limited (Krawchuk et al., 2009), increased carbon concentration in the atmosphere may reinforce the effect of climate on fire frequency and intensity (Langenfelds et al., 2002; Flannigan et al., 2006). Such increases are spatially variable. Furthermore, some areas may not experience changes with respect to current fire regimes, while others may even experience reduced fire occurrence (Flannigan et al., 2009; Kloster et al., 2012; Andela et al., 2017).

Given the relationship between the fire regime and climate, the Global Climate Observing System (GCOS) considers fire disturbance as an Essential Climatic Variable (ECV). An ECV is a physical, chemical, biological or a group of linked variables that contributes in a critical way to the characterization of the climate system, being key to study and predict its evolution (Bojinski et al., 2014). The origin of ECVs

* Corresponding author.
E-mail address: miguel.belenguer@uah.es (M.A. Belenguer-Plomer).

https://doi.org/10.1016/j.rse.2019.111345
Received 13 July 2018; Received in revised form 17 June 2019; Accepted 23 July 2019
Available online 09 August 2019

dates back to the 1990s, when gaps in climate knowledge and the reduction of observation networks in many countries led GCOS to develop the ECV concept to simplify the study of climate through systematic observations of a limited set of variables with great climatic importance using satellite remote sensing data (Hollmann et al., 2013; Bradley et al., 2012). In 2010, the European Space Agency (ESA) started the Climate Change Initiative (CCI) programme as the main contribution of the Agency to the GCOS agenda. The CCI programme aims to obtain information on different ECVs using remote sensing data to help in improving climate modelling (Plummer et al., 2017; Hollmann et al., 2013). Fire Disturbance is one of the ECV included in the first phase of the CCI programme initiated in 2010. The goals of this project were to produce long-term and consistent time series of global BA information (Chuvieco et al., 2016). The interest of global BA products for climate modelling has been reviewed by several authors (Mouillot et al., 2014; Poulter et al., 2015). And many global BA products have been released over the last years (Humber et al., 2018). Three such products were based on data from the NASA's Moderate Resolution Imaging Spectrometer (MODIS) sensor, the MCD45 (Roy et al., 2008), the MCD64 (Giglio et al., 2009, 2018) and the MODIS Fire_cci v5.0 (Chuvieco et al., 2018). Images acquired by the VEGETATION sensor on board the SPOT-4 (Satellite Pour Observation de la Terre) satellite have also been used to generate global BA products, namely the Global Burnt Area (GBA) 2000 (Tansey et al., 2004), Globcarbon (Plummer et al., 2006), L3JRC (Tansey et al., 2008) and the Copernicus Global Land Service Burnt Area (based on Proba-V since 2014: land.copernicus.eu/global/products/ba). Furthermore, the European Remote Sensing Satellite - Advanced Along Track Scanning Radiometer (ERS2-ATSR2) was used to generate the Globscar product (Simon et al., 2004) while the MEdium Resolution Imaging Spectrometer (MERIS) data were used to generate the Fire_cci v4.1 product (Alonso-Canas & Chuvieco, 2015; Chuvieco et al., 2016). All these products were obtained using passive remote sensing datasets (optical and thermal wavelengths) which have significant limitations in areas with persistent cloud cover. Another limitation comes from the relatively coarse (> 250 m) spatial resolutions of these sensors, which makes the detection of small fires difficult (Stroppiana et al., 2015a; Randerson et al., 2012).

Several factors limit burned area mapping from remote sensing data. These factors are related to both, the sensor characteristics and the observed scene. The type of sensor (passive or active) and the region of the electromagnetic spectrum in which the images are acquired are decisive in the success of the burned area detection. Among the scene characteristics influencing detection accuracy, the size and shape of fire patches, land cover type, fire unrelated changes (e.g., phenology, floods, harvest, insects) and the presence of clouds (optical and thermal part of the spectrum) are the most relevant. Since sensor and scene related factors interact, the degree to which each of the mentioned factors affect BA detection success varies (Eva & Lambin, 1998; Boschetti et al., 2004; Belenguer-Plomer et al., 2018a; Padilla et al., 2015). The spatial and temporal resolutions of the sensor have a significant impact on BA mapping accuracy, determining the minimum size of the fires that can be detected (Boschetti et al., 2004) and the time interval between fire and detection (Eva & Lambin, 1998). However, previous studies suggest that temporal resolution is less important than the spatial resolution when it comes to the accuracy of the BA detection (Boschetti et al., 2010).

In a survey based on a questionnaire of 47 researchers who used BA products and an extended literature review, Mouillot et al. (2014) suggested that BA products should have commission errors (CE) in the range of 4% (ideal) to 17 % (maximum) while omission errors (OE) above 19% were deemed less useful for the climate modelling efforts. A first global comparison analysis found that the NASA's MCD64 was the most accurate BA product (Padilla et al., 2015), but was far from achieving these goals with CE and OE reaching 42% and respectively 68%. These errors were in part due to the low spatial resolution which results in small fires being overlooked (Randerson et al., 2012). A recent study has demonstrated that the contribution of small fires may be in fact even greater, as comparing Sentinel-2 and MODIS products for Africa showed an underestimation of almost 45% of BA (Roteta et al., 2019). Therefore, the development of new BA detection algorithms is a relevant research topic in the current context where climate change is a key issue. To achieve this improvement, the use of images from new satellites, such as those of the Copernicus missions of ESA, is necessary. Furthermore, alternative mapping options (e.g., radar based) are needed over areas where optical images are limited by persistent cloud cover (e.g., tropical areas).

During the last decade, synthetic aperture radar (SAR) data have been increasingly used for BA mapping as data from multiple sensors became available. Such studies have taken advantage of radar independence of cloud cover and solar illumination, their increased spatial resolution and the availability of multiple polarizations and incidence angles (Bourgeau-Chavez et al., 2002; French et al., 1999). The European Remote Sensing (ERS) SAR satellites (ERS-1 and ERS-2) were widely used in boreal (Bourgeau-Chavez et al., 1997; Kasischke et al., 1994), tropical (Siegert & Hoffmann, 2000; Siegert & Ruecker, 2000; Ruecker & Siegert, 2000) and Mediterranean (Gimeno et al., 2004, 2002) ecosystems to detect and map BA. More recently, RADARSAT (Gimeno & San-Miguel-Ayanz, 2004; French et al., 1999) and ALOS - PALSAR (Advanced Land Observation Satellite Phased Array type L-band Synthetic Aperture Radar) (Polychronaki et al., 2013) were employed for the same purpose. However, past SAR missions only provided data with low temporal resolution which hindered the development of efficient radar-based BA detection and mapping algorithms over large areas. In addition, the utility of past sensors was limited by the available polarizations (mostly single co-polarized sensors), steep viewing geometries (far from ideal when monitoring changes in vegetation) and data access restrictions.

With the launch of ESA's Sentinel-1 satellite constellation (A and B platforms, operational since October 2014 and December of 2015, respectively) such limitations have been largely reduced. The Sentinel-1 constellation could theoretically provide images every three days by combining datasets acquired during ascending and descending trajectories. The independence from cloud cover and solar illumination, added to improvements in sensors characteristics (e.g., dual polarization, increased spatial resolution and incidence angle, precise orbital information), provides untapped opportunities for BA detection. A few studies have already explored the potentials of Sentinel-1 SAR images for BA detection, but these studies are focused on specific regions (Engelbrecht et al., 2017; Lohberger et al., 2018). To date, few studies tried integrating active and passive datasets for BA detection. Such a study detected BA independently from Sentinel-1 and Sentinel-2 datasets on a relatively small area in the Congo basin suggesting that a combined sensor approach compensates for the strengths and limitations of each individual sensor (Verhegghen et al., 2016). However, SAR based BA detection has limitations as discussed in more detail in Subsection 3.2. Lastly, fusion approaches combining optical and radar data have been considered for BA detection. In Stroppiana et al. (2015b,a) Landsat-5 TM and C-band ENVISAT ASAR data were integrated into a fuzzy algorithm aimed at burned area detection in a Mediterranean environment.

This paper presents a novel radar-based BA mapping algorithm based on temporal series of C-band backscatter coefficient, that self-adapts to local scattering conditions and it is able to detect small fires (down to 1 ha) in a fairly automatic way. The specific objectives of this study were to: (i) present the proposed algorithm and explain its functionalities; (ii) validate the BA detections over major biomes; (iii) compare the detection accuracy with that of existing products based on passive datasets; and (iv) analyse the factors influencing the algorithm accuracy.

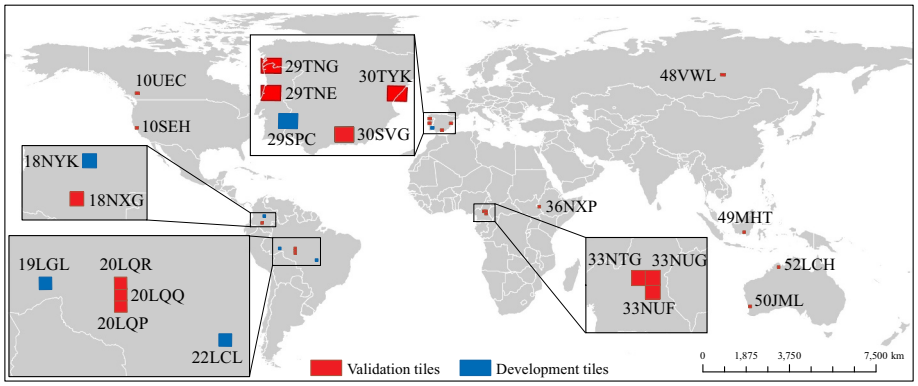

Fig. 1. Location of the Military Grid Reference System tiles used for algorithm development and validation.

2. Study area and dataset

The algorithm was developed using data from four sites, three located in the Amazon basin and one located in the Iberian Peninsula. Subsequently, the algorithm was validated over 18 sites around the world (Fig. 1). The validation areas were located within biomes where fire events occur frequently, from boreal forests to tropical and subtropical forests, savannas and grasslands.

The algorithm relies on temporal series of Ground Range Detected (GRD) dual-polarized (vertical-vertical VV, and vertical-horizontal VH polarizations) SAR images acquired by the Sentinel-1 A/B satellites in interferometric wide (IW) swath mode. The GRD data was processed on a tile base structure using as grid the 100 × 100 km Military Grid Reference System (MGRS). For each tile, Sentinel-1 images from ascending and descending passes (when available) and from all intersecting relative orbits were used. Land cover (LC) classification and hotspots derived from thermal anomalies were used as ancillary data.

The land cover classification was produced in the framework of the ESA's Land_Cover_cci project. This project delivers time series of consistent global LC maps at 300 m spacing on an annual basis from 1992 to 2015. The most recent map (i.e., 2015) was used. CCI land cover maps were generated using a combination of sensors, including MERIS and Proba-V time series of surface reflectance (Kirches et al., 2014). Since the SAR images were processed at a significantly higher pixel spacing (40 m, see Subsection 3.1) than the LC map, the latter was resized using a nearest-neighbour interpolation to coincide with the SAR spacing. In addition, the Land Cover Classification System (LCC) (Di Gregorio, 2005) was simplified by joining similar cover types into six groups: shrublands, grasslands, forests, crops, non-burnable, and others. One should notice that BA detection takes place over 100 × 100 km tiles. Therefore, for any given tile, the simplified LCC classification groups very similar classes.

Hotspots were available from NASA's Fire Information for Resource Management System (FIRMS). The hotspots were recorded by two sensors, the VIIRS (Visible Infrared Imaging Radiometer Suite) sensor at 375 m spatial resolution (Schroeder et al., 2014) and the MODIS sensor at 1 km spatial resolution (Giglio et al., 2003). The VIIRS and MODIS database was last accessed in January 2018.

To derive the validation fire perimeters (see Subsection 3.4 for more details), Landsat-8 optical images were retrieved from the United States Geological Survey repository (USGS) as atmospherically corrected surface reflectance products (Vermote et al., 2016). The validation period was adjusted for each tile considering the fire season length and the availability of Landsat images with a cloud cover under 30%. Sentinel-2 Level-1C images retrieved from the Copernicus Open Access Hub were considered to reduce temporal gaps in the validation dataset and thus large discrepancies between the validation period and the Sentinel-1 detection period.

The effect of soil moisture, an important factor affecting radar backscatter, on BA detection accuracy was analysed using the global Soil Moisture Active Passive (SMAP) product. Specifically, the Enhanced Level 3 Passive Soil Moisture Product based on L-Band Radiometer (9 km pixel spacing and 3 days revisit period) was used. The reliability of this product was demonstrated by a correlation coefficient above 0.8 between the estimated soil moisture and *in situ* measurements (Chan et al., 2018; Chen et al., 2018). From this product, the descending pass images (6 AM Equator crossing), more accurate than ascending according to Chan et al. (2018), were used so that all measurements represented the same acquisition time (Chan, 2016). As for the LC map, the product was resized to 40 m using the nearest-neighbour interpolation.

3. Methods

3.1. SAR data pre-processing

The Sentinel-1 data was processed using open-source libraries available in the Orfeo ToolBox (OTB), an image processing software developed by the National Centre for Space Studies (CNES), France (Inglada & Christophe, 2009). The OTB-based processing chain uses Ground Range Detected (GRD) Sentinel-1 images with the SAR data being tiled to 100 km using the MGRS system. The chain is highly scalable and autonomous once few parameters are set and includes the data download from Sentinel-1 repositories. The SAR data processing may be grouped in several steps including, pre-processing, geocoding and temporal filtering (Fig. 2).

The pre-processing step includes data download of the specified MGRS tiles and radiometric normalization to gamma nought (γ^0) using

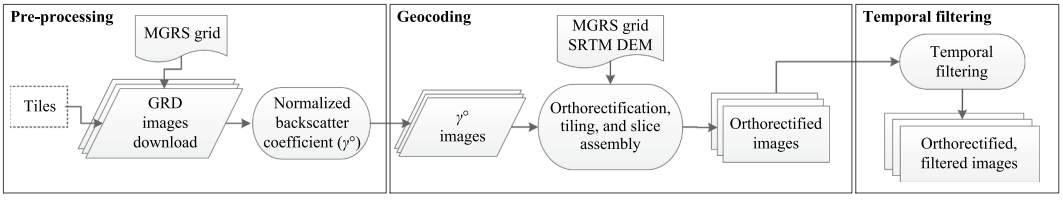

Fig. 2. SAR data processing with the Orfeo Toolbox.

the gamma nought lookup table provided in the product metadata. Only SAR images acquired in the interferometric wide swath mode, the Sentinel-1 default acquisition mode over land, were used. The calibrated images were orthorectified to ground geometry using elevation information from the Shuttle Radar Topography Mission (SRTM) one arc-second DEM and the bicubic interpolator. The orthorectified images were clipped to the processing tile and the data acquired from the same orbital path but provided within different slices were mosaicked (i.e., slice assembly). It should be noted that the BA algorithm uses temporal backscatter differences of the same relative orbit, hence, terrain-flattening (Small, 2011; Frey et al., 2013) was not necessary as the DEM-derived normalization (illumination) area for a given pixel is constant in time thus not affecting the pre- to post-fire backscatter coefficient variations (Tanase et al., 2010c, 2015, 2018). The last step was a multi-temporal filtering of the products for each satellite pass (Quegan et al., 2000). The GRD data were processed to the nominal Sentinel-1 resolution (20 m) through the OTB based chain.

The BA detection algorithm deployment over large areas is conditioned by its performance (speed) and accuracy. Both parameters are influenced by the pixel spacing to which products are processed as omission and commission errors are highly depended on speckle while the processing speed increases with decreasing pixel size. Analysing the effect of pixel spacing on image radiometric properties, processing time and BA detection accuracy were essential for selecting the optimum pixel spacing for deployment. Tanase & Belenguer-Plomer (2018) carried out an analysis for four pixel spacing (i.e., 20, 30, 40 and 50 m) over two test tiles. A 40 m spacing provided the optimum trade-off between speckle reduction, storage and computing requirements and the accuracy of the detected BA. Therefore, the temporally filtered images were aggregated to 40 m.

Radio Frequency Interference (RFI) may contaminate SAR data. Since RFI are largely observed over highly populated urban areas (Li et al., 2004; Njoku et al., 2005, Lacava et al., 2013) and considering that burned areas are usually located away from large cities, such effects were not observed and consequently were not considered.

3.2. Backscatter behaviour in burned areas

To better understand the proposed algorithm, its development, and the decision-making process that shaped it, this subsection describes the behaviour of C-band backscatter coefficient after fire events.

Fire on vegetated areas results in variations of the backscatter coefficient, which may increase or decrease depending on the polarization, the remaining vegetation and the environmental conditions (i.e., rainfall) during SAR data acquisition. Fire consumption reduces the number of vegetation scattering elements potentially reducing the backscatter coefficient (Van Zyl, 1993; Antikidis et al., 1998). However, biomass consumption may increase scattering from the ground due to reduced signal attenuation (less vegetation) and the increased effect of soil surface properties, such as moisture and roughness (Tanase et al., 2010b). Hence, microwaves backscatter behaviour in areas affected by fires may be more heavily influenced by soil moisture properties when compared to unburned areas, particularly when rainfall occurs after the fire (Imperatore et al., 2017; Gimeno & San-Miguel-Ayanz, 2004; Ruecker & Siegert, 2000). Rain and melting snow are the main causes of increased soil moisture (Huang & Siegert, 2006), influencing the radar signal and consequently reducing C-band sensitivity to fire induced changes (Tanase et al., 2010b). SAR-based BA mapping may be further hindered by spatial changes in soil moisture due to fire unrelated factors (e.g., temperature, insolation, wind, slope and orientation, soil roughness) which are difficult to embed into detection algorithms. The local incidence angle (LIA) is yet another factor influencing C-band sensitivity to fire induced changes, with smaller LIA values providing increased burned to non-burned differentiation for co-polarized waves (Gimeno & San-Miguel-Ayanz, 2004; Huang & Siegert, 2006; Tanase et al., 2010b). Finally, wave polarization is also a fundamental variable, with cross-polarized waves being more sensitive to changes in vegetation (volumetric scattering) and less to surface properties (e.g., soil moisture and roughness) when compared to the co-polarized waves (Freeman & Durden, 1998; Yamaguchi et al., 2005; Van Zyl et al., 2011). Such contrasting effects may generate a wide range of possible backscatter variations over burned areas that depend on the interplay between the SAR sensor characteristics (e.g., wavelength, polarization, incidence angle) and environmental conditions at SAR acquisition (e.g., fire impact, soil surface properties, meteorological conditions).

The impact of fire on the backscattering coefficient was actually found to cause ambiguous effects. A strong backscatter decrease was found for burned tropical forests at C-band VV polarization under dry weather conditions due to the decreased volume scattering and increased heat flux, which led to a dryer ground (Ruecker & Siegert, 2000; Lohberger et al., 2018). After rainfall, discrimination from the unburned surrounding forests was difficult as the backscatter coefficient over BA increased (Siegert & Ruecker, 2000). In the temperate region and the Mediterranean basin, lower backscatter values were found in fire-affected areas for cross-polarized C-band when compared to adjacent unburned forest (Rignot et al., 1999; Imperatore et al., 2017). In boreal forests, higher backscatter values, when compared to the adjacent unburned areas, were observed at C-band VV polarization when soil moisture was high, whereas lower backscatter was observed for sites with better drainage (Bourgeau-Chavez et al., 2002; Huang & Siegert, 2006; Kasischke et al., 1994). In Australian woodlands and open forests, the post-fire backscatter increased for co-polarized waves and decreased for cross-polarized waves (Menges et al., 2004) while for African open forests the backscatter decreased for both co- and cross-polarized C-band channels, although only the co-polarized channel was deemed useful for BA detection (Verhegghen et al., 2016). Changes in the post-fire backscatter levels appear to be strongly related to changes in soil moisture, with data acquired after rainfall being less suitable for classification or biophysical parameters retrieval. However, some fire-related studies reported increased differentiation potential for BA after rainfall in the Mediterranean basin (Gimeno & San-Miguel-Ayanz, 2004).

3.3. Burned area detection and mapping algorithm

The main requirements of the BA detection algorithm were: (i) the use of cloud insensitive satellite data (i.e., SAR); (ii) sensitivity to local burn conditions; and (iii) a high degree of automation. The algorithm was designed to make use of existing datasets for training purposes by using sets of susceptible burned and unburned pixels for locally dominant land cover types. The algorithm has six stages with its simplified structure being provided in Fig. 3. The following paragraphs explain in detail each stage.

3.3.1. Stage 1: Anomaly change detection

An anomalous change implies variations outside the typical behaviour expected for a given area and time. Burned areas were considered anomalies since fires are inconsistent spatial and temporal events. The Reed-Xiaoli detector (RXD), proposed by Reed & Yu (1990), extracts signatures that are distinct from the surroundings without the need for *a priori* information. Anomalies have two characteristics that make them outliers: (i) spectral signatures different from the surrounding pixels; and (ii) low occurrence probability (Stein et al., 2002; Banerjee et al., 2006; Kwon & Nasrabadi, 2005). Hence, RXD allows distinguishing anomalous changes, such as burned areas, from pervasive changes (e.g., seasonal effects) that occur periodically and extend over large swathes of the image (Theiler & Perkins, 2006). The RXD uses the covariance matrix to calculate the Mahalanobis distance from a given pixel to the mean of the surrounding (background) pixels (Dabbiru et al., 2012). Thus, for any given pixel, the anomalous change (AC) score is computed by the RXD (Eq. (1)).

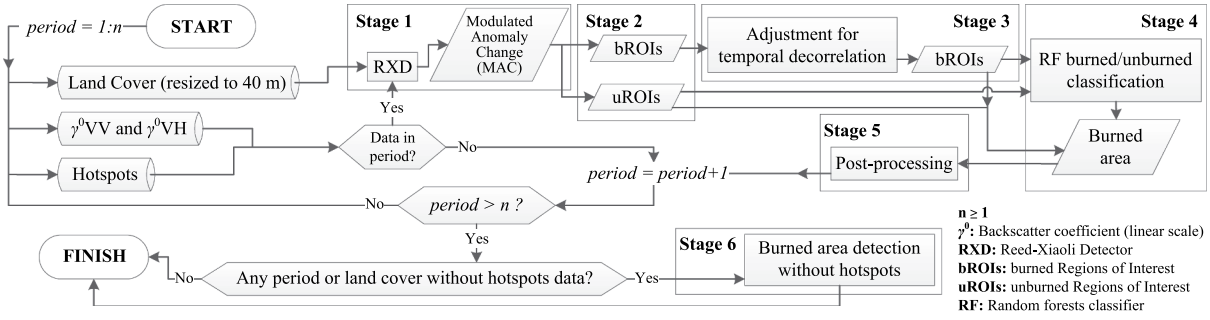

Fig. 3. Flowchart of the SAR based algorithm for burned area detection.

$$\mathrm{AC}(x) = (\mathbf{x'} - \boldsymbol{\mu})^{\top}\mathbf{C}^{-1}(\mathbf{x'} - \boldsymbol{\mu}) \quad (1)$$

where x is any given pixel, $\mathbf{x'}$ is a vector formed by the image bands values of the pixel x, $\boldsymbol{\mu}$ is a vector composed of the mean value of the background pixels (e.g., stable areas) in each image band and $\mathbf{C}$ is the covariance matrix of the image bands (computed from the background pixels). The background value may be computed as the mean sample of a subset image where only pixels of the same land cover class of x are included to differentiate anomalous changes from pervasive, since seasonal effects and soil moisture variations may affect the backscatter coefficient in a divergent way as a function of land cover class. When *a priori* information is available, the background value may be computed from areas where anomalies are not expected. For BA detection, *a priori* information was provided by MODIS and VIIRS active fire databases. MODIS and VIIRS hotspots corresponding to the current detection period (CDP) were used to mask areas likely affected by fires while the remaining pixels were used to calculate the background values. The BA masks were derived by taking a buffer of 0.75 km around each hotspot. This buffer was considered the influence area of each individual hotspot (IAhs) and it roughly corresponds to the pixel size for VIIRS and MODIS thermal channels while also considering location uncertainty.

The RXD was applied to a set of temporal ratios of the backscatter coefficient (Eqs. (2) and (3)). Such temporal indices were previously used for estimating the impact of different disturbance agents (e.g., fire, insects, wind) on vegetation (Tanase et al., 2015, 2018). The selected temporal radar indices mainly use the VH backscatter, which is more responsive to volumetric scattering from vegetation and less affected by changes in surface properties (e.g., soil moisture, surface roughness) when compared to the co-polarized (VV polarization) channel (Freeman & Durden, 1998; Yamaguchi et al., 2005; Van Zyl et al., 2011).

$$RI_1 = \gamma^0VH_{t-1}/\gamma^0VH_{t+1} \quad (2)$$

$$RI_2 = (\gamma^0VH_{t-1}/\gamma^0VV_{t-1})/(\gamma^0VH_{t+1}/\gamma^0VV_{t+1}) \quad (3)$$

where γ^0 is the backscatter coefficient (linear scale) of VV or VH polarizations, and $t-1$ and $t+1$ are respectively pre- and post-fire detection dates that define the CDP.

To reduce commission errors related to signal variation due to changes associated to post-fire events (e.g., vegetation regrowth), the AC values for CDP were modulated by the AC values recorded for the previous detection period (PDP) (Eq. (4)). Practically, AC scores of the PDP were subtracted from the AC of the CDP. The result was a Modulated Anomalous Changes (MAC) score used in all subsequent algorithm stages.

$$\mathrm{MAC}(x) = \mathrm{AC}(x)_{[t-1..t+1]} - \mathrm{AC}(x)_{[t-2..t-1]} \quad (4)$$

3.3.2. Stage 2: Burned and unburned regions of interest

In this stage, burned and unburned Regions of Interest (ROIs) were automatically extracted using the MAC scores and ancillary information from hotspots and land cover data. Since information on hotspots was acquired daily from two independent sensors (VIIRS and MODIS) most burned pixels in the selected study areas (94.3%) were in fire patches with at least one hotspot within 0.75 km, the selected buffer considered as hotspot area of influence (IAhs) even for the tropical regions, where cloud cover is frequent. The presence of hotspots greatly facilitated the attribution of the detected MAC values to burned areas. This allowed distinguishing BA from other changes, such as logging, crop harvesting, flooding, or vegetation disturbance due to insects or diseases. When hotspots were not available, due to the cloud cover or small fire size, a different attribution method was used as explained in Stage 4. Burned ROIs (bROIs) were extracted in two steps: seeding and growing. This is an approach previously used for BA mapping algorithms (Bastarrika et al., 2011; Alonso-Canas & Chuvieco, 2015; Roteta et al., 2019). To obtain the seeds, spatially connected IAhs pixels were first grouped in uniquely identified objects: $q_1{:}n$, where n is the number of the unique objects. A pixel x inside an object q, was considered burned seed (bSeed) if Eq. (5) was met.

$$\begin{aligned} x = \mathrm{bSeed}(q) \rightarrow & \\ & (\mathrm{MAC}(x) \geq \min(s, v) > 0) \vee (\mathrm{MAC}(x) \\ & \geq \max(s, v) > 0 \wedge \min(s, v) < 0) \end{aligned} \quad (5)$$

where $s = \mu(\mathrm{MAC}_{q'})$, μ being the mean and q' a region around q bounded by $dist_q$ and $dist_q + \sqrt{dist_q}$, with $dist_q$ being the maximum span of object q. Thus, q' delineates likely unburned areas in the vicinity of q; and $v = \mu(\mathrm{MAC}_{\mathcal{N}_G})$, with $\mathcal{N}_G$ being the neighbour pixels of G, where G is a pool of pixels inside q with MAC values below $\mu(\mathrm{MAC}_q)$. Essentially, for a pixel to be considered seed it had to fulfil two conditions, one related to vicinity to a hotspot (within IAhs) and the second related to the magnitude of backscatter change (MAC score).

The bSeed pixels were extracted considering the major land cover type for each q object. Therefore, pixels in q' region were stratified by land cover type with only pixels of the same land cover type as predominant of q being used for computations. In addition, the selected q' pixels needed to be outside the IAhs of any other hotspot. Fig. 4 shows graphically the concepts of q, q' and $dist_q$. Once bSeed pixels for q were extracted, an open morphological operator (3 × 3 window) was used to eliminate isolated bSeed pixels. With increasing window size, BA omission errors increased while commission errors decreased. To determine the optimum size, an error analysis was carried out using different window sizes (3 × 3, 5 × 5 and 7 × 7) over the four algorithm development tiles (analysis not shown). The 3 × 3 window was selected since it least affected the detection of small size fires while still managing to reduce commission errors. The same window size was used in previous works to reduce speckle effects (Menges et al., 2004).

Given an object q and its predominant land cover class k, the growing phase started by masking out all the pixels of the image which MAC values were below the mean MAC value of all image pixels of land cover class k. The remaining pixels were used to compute a new mean of the MAC values which was used as the minimum threshold to label Likely Burned Pixels (LBP) of q (Eq. (6)).

$$x = \mathrm{LBP}(q) \rightarrow \mathrm{MAC}(x) > \mu(MAC > \mu(MAC_k)) \quad (6)$$

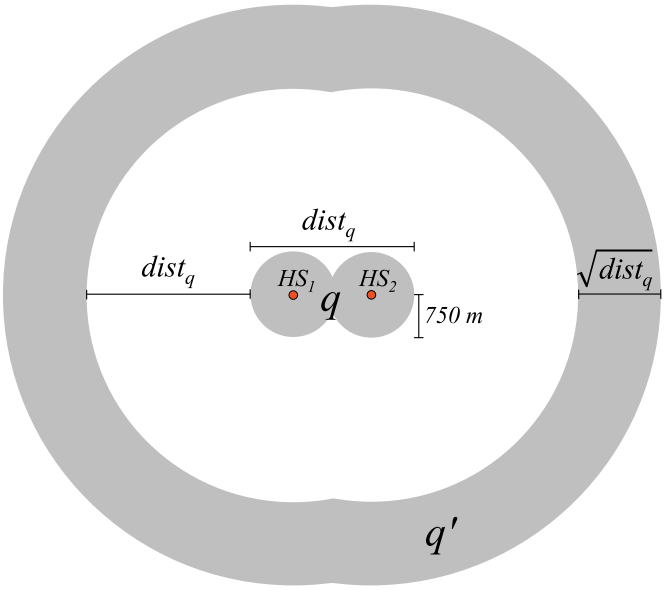

Fig. 4. Graphical representation of concepts needed to extract bROIs, being *HS* - hotspot.

Connected LBP(q) pixels were grouped and subsequently overlapped with the extracted bSeed pixels of q. LBP(q) groups overlapping bSeed pixels of q were assigned to the bROIs and constituted the first component of the detected burned areas. The second component was detected using no parametric classification (i.e., random forests) as explained in Stage 4.

The unburned ROIs (uROIs) were derived iteratively by land cover type. The histogram of bROIs pixels identified in the previous step was used to calculate the MAC values for the 25 and 75 percentiles (P_{25} and P_{75}, respectively). These values constituted thresholds used to classify the MAC image in burned and unburned. Pixels with MAC values below P_{25} or above P_{75} were considered possible unburned seeds since: (i) MAC values below P_{25} indicate small changes, likely unrelated to fires (e.g., vegetation growth, changes in vegetation water content); and (ii) MAC values above P_{75} are usually associated with significant changes, such as logging, crop harvesting, or floods. One should note that, high severity fires may also result in MAC values above P_{75}. However, such areas are regularly associated to hotspots and therefore were not labelled as uROIs. An open morphological operator (3 × 3 window) was applied to the classified binary image to remove noise. The effect of the open morphological operator was an increased number of unburned pixels. Pixels from the not burnable LC map classes (i.e., bare soils, water, snow and ice, urban areas) were labelled as uROIs, while pixels overlapping IAhs or bROIs were filtered out. Additionally, for the crop land cover class, groups of pixels over 56 ha (0.75 × 0.75 km, 0.75 km being the double of VIIRS spatial resolution) not overlapping hotspots were included as uROIs to account for fire-unrelated changes, such as crop harvesting or changes in surface properties (roughness) due to agricultural works (e.g., ploughing).

3.3.3. Stage 3: Adjustment for temporal decorrelation

During algorithm development, a temporal decorrelation between fire events (i.e., hotspots date) and backscatter coefficient change was observed (Belenguer-Plomer et al., 2018b). Such decorrelation events may be the result of delayed backscatter decrease after fire due to multiple factors including: (i) pre-fire conditions, e.g., drier than usual weather may result in low values for the pre-fire backscatter coefficient; (ii) post-fire weather, e.g., precipitations may temporally increase the backscatter coefficient; and (iii) vegetation-dependent backscatter response to fire events. For example, over forests, VH backscatter decrease may be delayed as there are still sufficient scattering elements (tree trunks and branches) present after fire. As time passes, trunks and branches dry up, which results in decreased backscatter from vegetation.

To account for temporal decorrelation the BA was detected iteratively for each period. Delayed changes in backscatter were accounted for computing the bROIs detected in periods formed by the current pre-fire image ($t - 1$) and images acquired during the following 90 days past the CDP (i.e., $t + 2$, $t + 3$, ...). This temporal threshold was based on empirical observations (Belenguer-Plomer et al., 2018b). Such bROIs were labelled as burned in the CDP ($t - 1$ to $t + 1$) when overlapping hotspots from the CDP. Additionally, these bROIs must not overlap hotspot recorded past the CDP.

3.3.4. Stage 4: Random forests burned/unburned classification

Only a fraction of the anomalous pixels was labelled as burned based on information from hotspots due to the rather restrictive criteria (i.e., MAC score) used in Stage 2 and 3. Pixels not meeting the imposed criteria also needed labelling. To avoid subjectivity, such pixels were labelled using a non-parametric classifier (i.e., random forests) trained with data extracted from bROIs and uROIs by each land cover classes and CDP. The random forests (RF) classifier was used as it is robust to data noise (Gislason et al., 2006; Rodriguez-Galiano et al., 2012; Du et al., 2015; Waske & Braun, 2009) and less sensitive, when compared to other machine learning techniques, to the quality of training samples and overfitting (Belgiu & Drăguţ, 2016). Moreover, RF was already used to classify SAR data (Waske & Braun, 2009) and solve similar fire mapping problems (Collins et al., 2018; Fernandez-Carrillo et al., 2018; Ramo & Chuvieco, 2017; Meddens et al., 2016).

RF is an ensemble classifier that consists of a group of decision trees $\{h(\mathbf{x}', \Theta_z), z = 1, ...\}$, where $\mathbf{x}'$ is the input vector of any given pixel (x), and Θ_z are an independently bootstrap sampled vectors with replacement in each decision tree (z). Each tree provides a unique class for x, being the class of x assigned as the most popular voted class (Breiman, 2001). In this study, *TreeBagger* from MATLAB® software package was used to construct the RF classifiers.

RF classifiers are customizable through different parameters, such as: (i) number of trees; (ii) number of training samples; (iii) proportion of training samples by class; and (iv) number of independent variables employed in each tree. The number of trees is a key adjustment in RF classification since for more trees the generalization error converges and models are not over-fit (Breiman, 2001; Pal, 2005; Rodriguez-Galiano et al., 2012). On the other hand, using more trees demands more computational resources. An empirical analysis (not shown) concluded that 250 trees provided the best trade-off between speed and accuracy for BA classification in this study. Since the number of pixels in bROIs and uROIs is high, computational costs may be reduced by using just a fraction for training purposes. This fraction was determined, by land cover classes, as 1% of all bROIs and uROIs pixels divided by the number of trees (250). Unbalanced training samples may result in infra-classification of the minority classes. According to Chen et al. (2004), several approaches may be used to address such problems: (i) reducing the overall learning cost, with high costs being assigned to the miss-classification of the minority classes (Pazzani et al., 1994); (ii) under-sampling the majority and over-sampling the minority classes; or (iii) a combination of both techniques (Chawla et al., 2002). The latter approach was used in this study. Depending on the misclassification cost, the *TreeBagger* function generated in-bag samples by oversampling the burned class and under sampling the unburned class. The proportion of training data was empirically adjusted to 40% and 60% for burned and unburned classes, respectively.

The number of variables considered for trees growing in each split was computed as the square root of the total number of variables (Gislason et al., 2006), as it reduces the correlation of trees and thus improves global accuracy (Rodriguez-Galiano et al., 2012; Gislason et al., 2006). In addition to the SAR based metrics used for RXD (Eqs. (2) and (3)), up to 30 SAR metrics were used for RF classification. These

metrics were computed as in Eqs. (7) to (12). The non-parametric classification was carried out considering the land cover type with specific models being built for each land cover class. The BA detected by RF was added to bROIs detected in Stage 2 and 3, and formed the total BA for the CDP.

$$\mu(\gamma^0XY_{[t',t-1]}) - \gamma^0XY_{t+i} \quad (7)$$

$$\mu(\gamma^0XY_{[t',t-1]})/\gamma^0XY_{t+i} \quad (8)$$

$$\gamma^0XY_{t-1} - \gamma^0XY_{t+i} \quad (9)$$

$$\gamma^0XY_{t-1}/\gamma^0XY_{t+i} \quad (10)$$

$$(\gamma^0VH_{t-1}/\gamma^0VV_{t-1})/(\gamma^0VH_{t+i}/\gamma^0VV_{t+i}) \quad (11)$$

$$\mu(\gamma^0VH_{[t',t-1]}/\gamma^0VV_{[t',t-1]})/(\gamma^0VH_{t+i}/\gamma^0VV_{t+i}) \quad (12)$$

where γ^0XY is the backscatter intensity (linear scale) of VV and VH polarizations, t' is $t-1$ minus the double of days distance between $t-1$ and $t+1$, and i is 1 or 2, 30 being the maximum number of indices computed.

3.3.5. Stage 5: Post-processing

Post-processing was needed to account for temporal decorrelation and improve detection results over problematic land covers such as cropping areas. To adjust for temporal decorrelation, the BA detected by the non-parametric classifier for the CDP was compared to the IAhs of previous detection periods, up to 90 days before the pre-fire image ($t-1$) (Belenguer-Plomer et al., 2018b). If burned areas detected in the current CDP (i.e., objects formed by contiguous pixels) overlapped previous IAhs (objects) by more than 75% (set from empirical observations) they were masked out and considered previous burns. Three additional post-processing steps were then carried out to further improve the results: (i) on cropping lands, groups of burned pixels (objects) with areas above 56 ha (see Stage 2) that did not overlap IAhs (i.e., no local hotspot) were removed. The rationale was that lack of hotspots over a large changing cropping area is an indication of harvesting rather than fire; (ii) burned objects below one hectare were removed to reduce noise in BA detections due to residual speckle; and (iii) a modal filter with a convolution kernel of 3 × 3 pixels was applied to smooth the salt and pepper effects typical for SAR based classifications.

Post-processing also deals with joining the BA detected in the different relative orbits intersecting a specific tile. The BA was detected separately for each relative orbit, to avoid misinterpreting backscatter changes due to changing azimuth angles or illumination geometry as fire related changes. To reduce topographic related effects such as layover, foreshortening and shadowing, burned areas detected in different relative orbits (i.e., from ascending and descending passes) were joined to obtain the final BA maps.

3.3.6. Stage 6: Burned area detection without hotspots

As clouds may prevent the propagation of radiation from active fires to the thermal sensors on board satellites, the algorithm was built with a backup mechanism to cope with the absence of hotspots for a specific land cover type and detection period. However, for the algorithm to work, hotspots need to be available for each land cover class at some point during the analysed fire season.

The algorithm first detected the BA for all land cover types during detection periods for which hotspots were available. For detection periods without hotspots, the data were temporally stored for later processing. During detection, the algorithm saved a database containing the P_{25} and P_{75} of MAC values for bROIs (Stage 2) and the trained RF models (Stage 4) for each land cover class. This database is hereafter referred to as the Classifier Model and Criteria (CMC). Once detections for land cover classes and detection periods with hotspots ended, the CMC database was used to classify the temporally stored data (i.e., land cover types without hotspots during detection periods) if two conditions were met: (i) the CDP was within the fire season. The length of the fire season was computed using the hotspots daily frequency as the interval between the dates corresponding to the P_5 and P_{95}; and (ii) the difference between the CDP and the date for the nearest CMC was less than one month, thus avoiding possible confusions due to changes in vegetation phenology. When CMC entries from different detection periods met the conditions, the one closest to the CDP was used. The MAC image for the CDP was segmented into possibly burned and unburned based on the CMC P_{25} and P_{75}, with the possible burned pixels being subsequently classified using the stored RF models by land cover class. When CMC entries were spaced equally in time when compared to the CDP (i.e., one entry is from a previous period and one from a posterior period), each entry was used separately and only the commonly detected BA was kept. The post-processing operations from Stage 5 were carried out on the detected BA from this stage.

An additional operation was carried out to reduce possible commission errors during this stage. The operation was carried out over BA detected on different relative orbits. Note that detections were always carried out using time-series of images from the same relative orbit. If several relative orbits intersected a given tile, the algorithm worked through the data from each relative orbit separately. BA products composites were subsequently formed using detections from different relative orbits and the same detection period. For each detection period, BA pixels detected in different relative orbits were grouped in objects. If all pixels of an object were classified as unburned in one orbit, the object was removed from the detected BA for the CDP. Since, dual pass (ascending and descending) acquisitions were not available for all tiles and spatially overlapping relative orbits only partially covered any given tile, this additional operation reduced commission errors where BA detections intersected.

3.4. Reference images and validation metrics

The reference burned perimeters extraction for validation purposes was based on a well established framework (Padilla et al., 2014, 2015, 2017). The reference data were obtained from Landsat-8 images using a RF classifier and training polygons selected by an independent operator. The validation perimeters were generated from 120 multi-temporal pairs of images with a maximum separation of 32 days. The temporal separation of the pairs was short to ensure that fire scars were clearly visible in the post-fire image. Before running the classification, clouds were removed using the pixel quality band of the Landsat product and each pair of images was clipped to the extent of its corresponding MGRS tile. Training areas were selected using a false colour composite (RGB: SWIR, NIR, R) that allowed for a clear discrimination of burned areas. Three training classes were considered: burned, unburned and no data.

The variables selected as input for the RF classifier were: (i) Landsat-8 bands 4 and 7; (ii) the Normalized Burn Ratio (NBR); and (iii) the temporal difference between the pre- and post-fire NBR values (dNBR). The NBR (Eq. (13)) is defined as the normalized difference between the reflectance of NIR and SWIR wavelengths (García & Caselles, 1991; Key & Benson, 2006).

$$\mathrm{NBR} = (\mathrm{Band4} - \mathrm{Band7})/(\mathrm{Band4} + \mathrm{Band7}) \quad (13)$$

where Band 4 is the surface reflectance in the near infra-red (NIR) wavelength (0.772–0.898 μm) and Band 7 is the surface reflectance in the shortwave infra-red (SWIR) wavelength (2.064–2.345 μm).

After the RF classification, fire perimeters were visually revised to correct possible errors. New training fields were iteratively added and the RF was re-run until the classification results were deemed accurate. Reference BA perimeters were resized using a nearest-neighbour interpolation to the selected pixel spacing of the Sentinel-1 product (40 m). Temporal gaps between the Landsat-8 reference period and the Sentinel-1 detection period were filled in through photo-interpretation

of Sentinel-2 images.

The Sentinel-1 BA detections were validated using confusion matrices (Table 1). Three accuracy metrics were computed for the burned area class using the confusion matrices, the omission error (Eq. (14)), the commission error (Eq. (15)) and the Dice coefficient (Eq. (16)) (Padilla et al., 2015).

Table 1
Confusion matrix example.

	Reference data		
Detection	Burned	Unburned	Row total
Burned	P_{11}	P_{12}	P_{1+}
Unburned	P_{21}	P_{22}	P_{2+}
Col. total	P_{+1}	P_{+2}	N

$$OE = P_{21}/P_{+1} \quad (14)$$

$$CE = P_{12}/P_{1+} \quad (15)$$

$$DC = 2P_{11}/(P_{1+} + P_{+1}) \quad (16)$$

4. Results

4.1. Algorithm accuracy

The OE and CE over the validation tiles varied, with the highest errors (0.54 to 0.81) being observed over Australian grasslands and the lowest (0.19 to 0.2) over the Mediterranean forests and shrublands (Table 2). The highest BA detection accuracy (DC 0.82) was observed over the tile 22LQP located in the Amazon basin (Fig. 5). By land cover type, the algorithm produces more accurate results over forested areas (DC 0.64), followed by shrublands (DC 0.56). The lowest detection accuracy was observed over grasslands (DC 0.28) (Fig. 6). Note that error metrics by land cover type were computed by pooling pixels with the same land cover type from all tiles.

4.2. Comparison with existing global products

The accuracy metrics of the Sentinel-1 BA detections obtained from the presented algorithm were compared to those derived from the current most widely used BA global product, the MCD64A1 Version 6 (Giglio et al., 2018). The magnitude of the error metrics may be influenced by the temporal match between the images used to generate the reference perimeters and those used to generate the BA products. To account for detection errors caused by slightly different validation and detection periods, the MCD64A1 product was temporally subset to match the Sentinel-1 detection periods.

The accuracy metrics were analysed by tile as well as by land cover classes. The tile-based analysis showed particularly poor results for the MCD64A1 product over the tiles 18NXG, 20LQQ, 20LQR, 30TYK, 33NTG, 33NUF and 33NUG (Fig. 6). For the remaining tiles, the accuracy of the two BA detection algorithms was closely matched, with some tiles being more accurately estimated by the Sentinel-1 algorithm while others by the MCD64A1. By land cover class, the MCD64A1 achieved higher accuracies over grasslands while the Sentinel-1 detections were considerably more accurate over forests. For the remaining land cover classes both products showed similar accuracies over burned areas. Overall, the BA was more accurately detected using the SAR based algorithm. On average Sentinel-1 detections improved the DC of the MCD64A1 product from 0.46 ± 0.11 to 0.59 ± 0.06 (± confidence interval, 95%) and reduced the OE from 0.55 ± 0.14 to 0.43 ± 0.08 and CE from 0.43 ± 0.08 to 0.37 ± 0.06 (Fig. 7).

4.3. Factors influencing the algorithm accuracy

The MAC values (Eq. (4)), and the temporal variation (pre- minus post-fire date) of backscatter coefficient and soil moisture were analysed by land cover class for each Sentinel-1 temporal pair after the BA classification. Four categories were studied: burned, unburned, commission and omission errors. Data from all tiles were pooled (Fig 8). The analysis confirmed that, over burned and commission error pixels, VH backscatter mean variation was higher (1.72 ± 0.002 dB) when compared to the VV polarization (0.34 ± 0.0023 dB) for all land cover classes. As expected, MAC values were on average considerably higher over burned pixels and commission errors (13.5 ± 0.15) when compared to unburned and omission errors pixels (0.17 ± 0.03), following the trends observed for VH backscatter coefficient mean variation. Soil moisture variations from the SMAP product were very similar between burned and unburned pixels with no particular trend being apparent. For crops and shrubs soil moisture variations were slightly higher over burned areas while for the other land cover classes the opposite was

Table 2
Error metrics for Sentinel-1 burned area detections for each MGRS tile analysed.

MGRS	Reference period	Detection period	P	Dd	nIM	LC	C	DC	OE	CE
10SEH	04/10/2017–05/11/2017	28/09/2017–03/11/2017	B	12	16	G	NA	0.61	0.34	0.43
10UEC	05/07/2017–22/08/2017	08/07/2017–25/08/2017	B	12	32	F	NA	0.76	0.31	0.16
18NXG	30/10/2016–02/03/2017	03/11/2016–03/03/2017	A	24	6	F	SA	0.64	0.35	0.36
20LQP	20/07/2016–22/09/2016	03/07/2016–25/09/2016	D	84	4	F	SA	0.82	0.14	0.22
20LQQ	04/07/2016–22/09/2016	03/07/2016–25/09/2016	D	36	5	F	SA	0.55	0.42	0.48
20LQR	04/07/2016–25/09/2016	03/07/2016–25/09/2016	D	36	8	F	SA	0.64	0.26	0.43
29TNE	05/10/2017–06/11/2017	04/10/2017–04/11/2017	B	6	24	S	Eu	0.7	0.38	0.2
29TNG	05/10/2017–06/11/2017	04/10/2017–05/11/2017	B	6	24	S	Eu	0.67	0.36	0.3
30SVG	30/06/2015–16/07/2015	26/06/2015–20/07/2015	B	12	9	S	Eu	0.65	0.19	0.46
30TYK	12/06/2017–30/07/2017	10/06/2017–28/07/2017	B	12	26	S	Eu	0.69	0.31	0.3
33NTG	28/11/2015–16/02/2016	21/11/2015–13/02/2016	A	12	14	F	Af	0.63	0.47	0.21
33NUF	07/12/2015–23/12/2015	28/11/2015–22/12/2015	A	12	3	F	Af	0.52	0.52	0.43
33NUG	21/11/2015–24/01/2016	16/11/2015–27/01/2016	A	12	8	F	Af	0.52	0.52	0.44
36NXP	30/12/2016–15/01/2017	01/01/2017–26/01/2017	D	6	6	S	Af	0.46	0.62	0.41
48VWL	12/06/2017–21/06/2017	11/06/2017–23/06/2017	D	12	3	F	As	0.58	0.57	0.15
49MHT	02/07/2015–04/09/2015	26/06/2015–06/09/2015	D	24	5	O	As	0.67	0.35	0.32
50JML	07/03/2017–10/05/2017	04/03/2017–15/05/2017	D	12	13	G	Au	0.21	0.81	0.76
52LCH	05/04/2017–21/04/2017	26/03/2017–24/04/2017	D	12	7	S	Au	0.31	0.78	0.51

Reference period - period for which the reference burn perimeter were derived; Detection period - first and last Sentinel-1 images of the data series; P - satellite pass (A-ascending, D-descending, and B-both); Dd - day difference between images (mode); nIM - number of SAR images within the detection period; LC - predominant land cover (G-grassland, S-shrub, F-forest, and O-others); C - continent for each tile (NA-North America, SA-South America, Eu-Europe, Af-Africa, As-Asia, and Au-Australia); DC - Dice coefficient; OE - omission error; and CE - commission error.

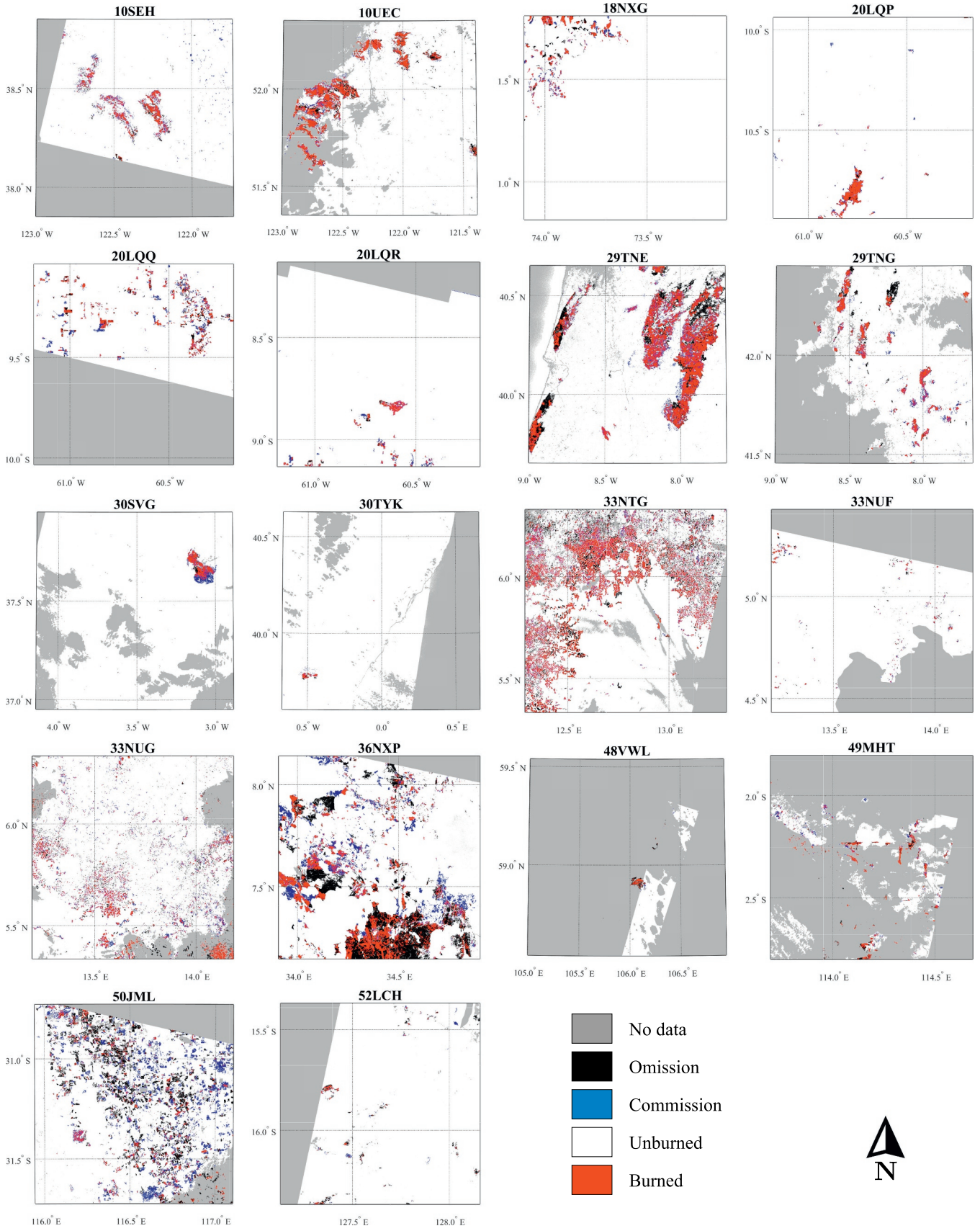

Fig. 5. Maps of burned area detected using Sentinel-1 data per MGRS tiles. Errors of omission and commission are also shown.

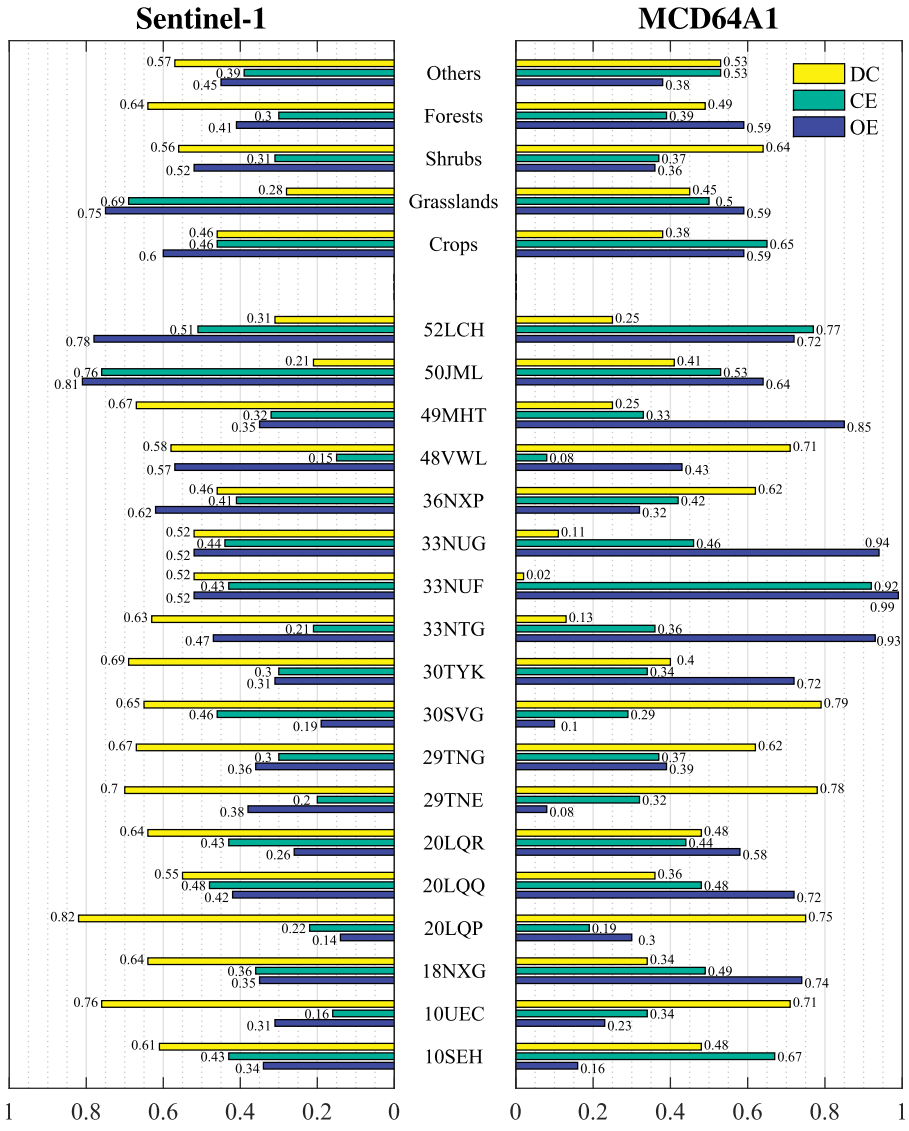

Fig. 6. Assessment metrics of Sentinel-1 and MCD64A1 Version 6 burned area detections per MGRS tiles and land cover classes. The metrics by land cover were computed using confusion matrices formed by pixels of the same land cover class from all tiles. DC - Dice coefficient, OE - omission error and CE - commission error.

true (Fig. 8).

Since the algorithm uses hotspots derived from thermal sensors to map BA, the accuracies metrics (by land cover class) of the pixels located within and outside the IAhs were also compared (Table 3). The highest BA accuracy (DC) and lowest omission and commission errors were observed for the pixels located within the IAhs over all land cover classes as expected. Likewise, VH and VV pre- to post-fire backscatter coefficient temporal differences were also compared for both cases. Similar trends, as observed in Fig. 8, where burned and commission error pixels had a significant higher variation when compared to unburned and omission errors pixels, were found over both polarizations independently of the location with respect to the IAhs.

For six of the validation sites, images from ascending and descending Sentinel-1 passes were available. Therefore, a more detailed

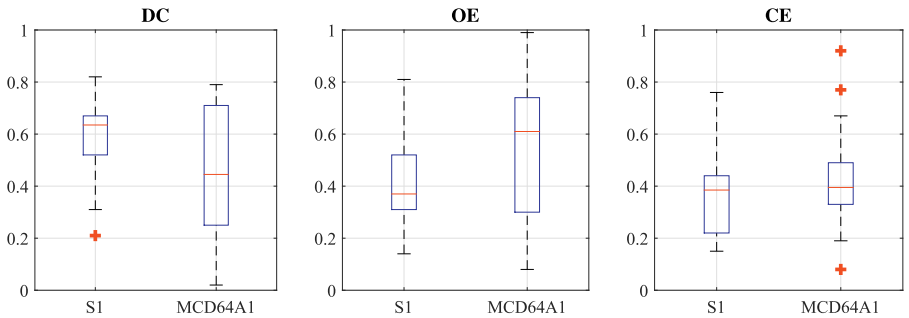

Fig. 7. Dispersion of Dice coefficient (DC), omission and commission errors (OE and CE) of burned area detected for all tiles for Sentinel-1 (S1) and MCD64A1 Version 6. The red line indicates median value, and top and bottom box edges indicate the 75th and 25th percentiles, respectively, while red dots indicate outliers.

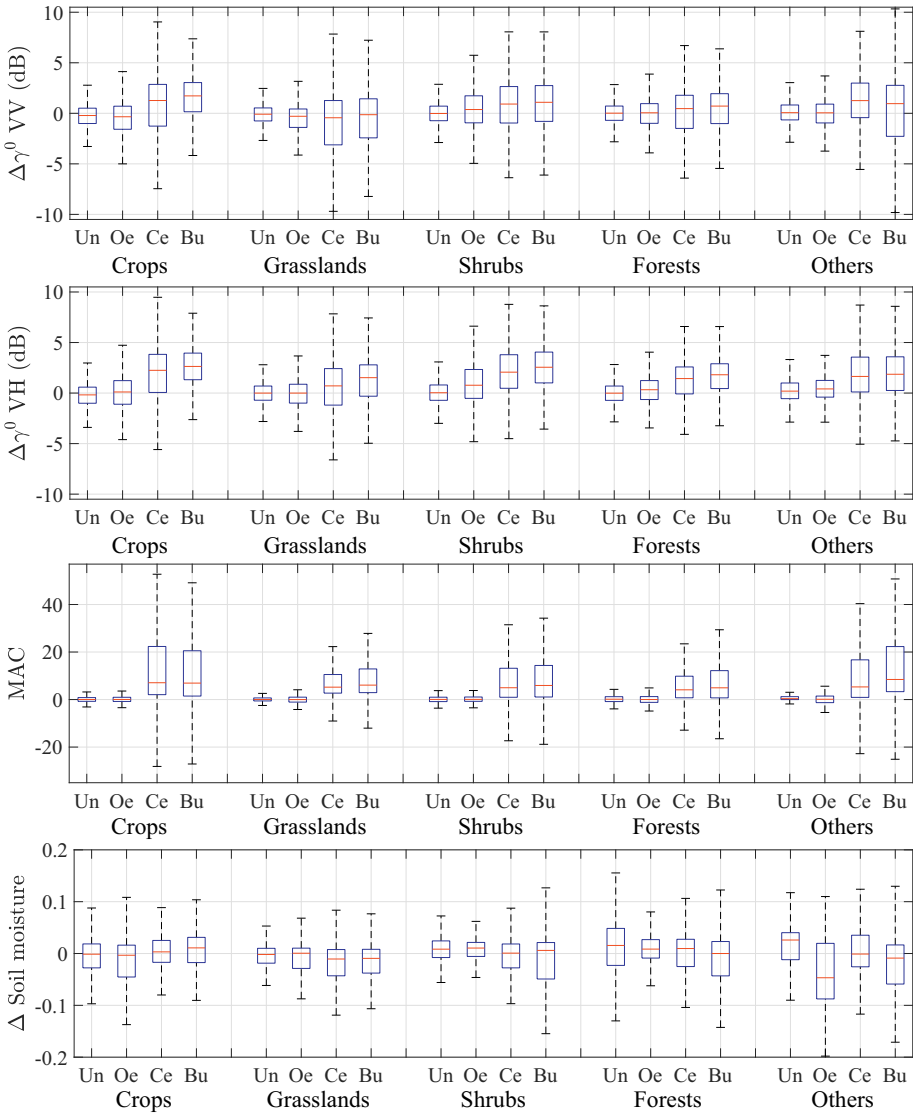

Fig. 8. Temporal variation ($\Delta = data_{pre} - data_{post}$) of the backscatter coefficient (dB) and soil moisture (from SMAP) between pre- and post-dates for BA detection periods. MAC values from RXD are also presented. Values are displayed by land cover classes for four categories of pixels: unburned (Un), burned (Bu) and commission (Ce) and omission errors (Oe). Red line indicates median value. Top and bottom box edges indicate the 75th and respectively the 25th percentiles. Outliers not shown to improved graphs discernibility.

analysis was carried out to understand the difference in BA accuracy between ascending and descending passes (Fig. 9). Overall, BA omission errors were minimum when both passes were used while BA commission errors increased. However, DC values showed that BA detection generally improved when data from both passes was available.

The effect of topography and the environmental conditions (soil moisture) were analysed for each acquisition pass over the six tiles. The LIA was often used to analyse the effect of topography on the backscatter coefficient in areas affected by fires (Tanase et al., 2010a, 2009; Kalogirou et al., 2014; Gimeno & San-Miguel-Ayanz, 2004; Kurum, 2015). However, the wide swath of the Sentinel-1 IW mode results in a variation of the incidence angle of about 17° from near (29°) to far (46°) range. Since LIA is a function of incidence angle and local slope (U), DC scores were analysed (by satellite pass) as a function of both angles after grouping in five degrees classes (Tanase et al., 2010a). Similar trends were observed for both passes (Fig. 10) with better accuracies being observed for low LIAs and Us groups (< 40°).

Nevertheless, analysing BA accuracy by LIA and U angles has limitations as LIA groups may include areas of different slopes while U groups may include slopes oriented towards and away from the sensor with completely different scattering properties. Therefore, the sloped areas (U ≥ 5°) were further analysed by their orientation (V) with respect to the satellite viewing geometry (Fig. 10). Notice that positive V values are observed for slopes oriented towards the sensor while negative values are observed for slopes oriented away from the sensor. The BA accuracy improved over pixels oriented toward the sensor with omission error being lower for such pixels while commission errors slightly higher. Notice that a paired t-test showed no significant difference (p-value > 0.05) between the percentage of pixels (by ten degrees V groups) from ascending and descending satellite passes.

Since Sentinel-1 ascending and descending images were acquired at different dates, variations in soil moisture (from the global SMAP product) between the pre- and post-dates delineating the CDPs were analysed to ascertain the influence of this important environmental parameter on BA detection errors. Over five of the six tiles the difference in soil moisture between ascending and descending passes was reduced. However, for tile 30SVG soil moisture increased considerably over some areas for descending pass acquisitions which translated in much larger commission errors (0.46) when compared to those observed for the ascending pass (0.16), where soil moisture was stable (Fig. 11). The

Table 3
Errors metrics for Sentinel-1 BA detections and pre- to post-fire backscatter variations assessed as a function of proximity with respect to the hotspots influence area (IAhs).

		Crops	Grasslands	Shrubs	Forests	Others
Inside IAhs	DC	0.55	0.34	0.63	0.71	0.61
	CE	0.38	0.64	0.27	0.27	0.36
	OE	0.5	0.68	0.45	0.32	0.43
	ΔVH (bp)	2.52 ± 0.02	1.06 ± 0.01	2.24 ± 0.005	1.48 ± 0.003	2.33 ± 0.03
	ΔVH (cp)	1.27 ± 0.03	0.64 ± 0.01	1.54 ± 0.01	0.91 ± 0.01	1.26 ± 0.03
	ΔVH (op)	0.15 ± 0.01	−0.33 ± 0.01	0.98 ± 0.003	0.31 ± 0.002	0.43 ± 0.01
	ΔVV (bp)	1.42 ± 0.02	−0.73 ± 0.02	0.66 ± 0.01	0.26 ± 0.003	0.84 ± 0.04
	ΔVV (cp)	0.03 ± 0.03	−0.91 ± 0.01	0.21 ± 0.01	−0.13 ± 0.01	0.42 ± 0.04
	ΔVV (op)	−0.29 ± 0.01	−0.78 ± 0.01	0.61 ± 0.004	0.06 ± 0.002	−0.1 ± 0.01
Outside IAhs	DC	0.11	0.17	0.39	0.27	0.45
	CE	0.84	0.79	0.44	0.56	0.54
	OE	0.92	0.86	0.7	0.81	0.57
	ΔVH (bp)	2.6 ± 0.09	1.2 ± 0.03	3.63 ± 0.01	2.25 ± 0.01	0.9 ± 0.05
	ΔVH (cp)	3.31 ± 0.04	0.33 ± 0.02	3.39 ± 0.01	2.18 ± 0.02	3.33 ± 0.08
	ΔVH (op)	−0.01 ± 0.02	0.08 ± 0.01	0.81 ± 0.01	0.22 ± 0.004	0.52 ± 0.02
	ΔVV (bp)	0.46 ± 0.11	−0.53 ± 0.03	1.73 ± 0.01	0.27 ± 0.02	−1.44 ± 0.07
	ΔVV (cp)	2 ± 0.05	−1.34 ± 0.02	2.03 ± 0.01	1.21 ± 0.02	2.78 ± 0.09
	ΔVV (op)	−0.73 ± 0.02	−0.55 ± 0.01	0.12 ± 0.01	−0.39 ± 0.005	−0.03 ± 0.02

Δ- pre- to post-fire temporal differences (pre- minus post-) of VV and VH backscatter data by pixels classes of: burned (bp) and commission (cp) and omission (op) errors.

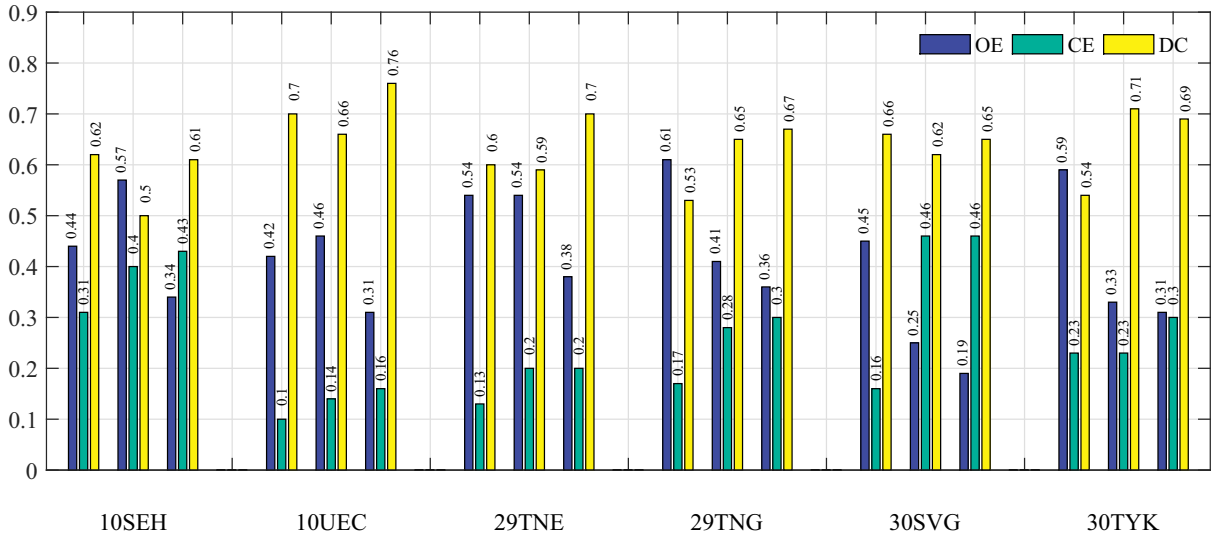

Fig. 9. Assessment metrics of Sentinel-1 burned area detections per ascending (A), descending (D) and both satellite passes (B). DC - Dice coefficient, OE - omission error and CE - commission error.

increased commission errors were the result of a large and compact area located south of the fire perimeter that was misclassified as burned (Fig. 12). The temporal variations of the backscatter coefficient between ascending and descending passes (tile 30SVG) were correlated with the accuracy metrics. An important variation of the backscatter coefficient during the descending pass was observed over the misclassified burned area (CE) for both VV (2.8 ± 0.029) and VH (1.0 ± 0.027) polarizations (Fig. 12).

5. Discussion

5.1. Algorithm development

The Reed-Xiaoli anomaly detector (Reed & Yu, 1990), not widely used with SAR images except for levee slide detection (Dabbiru et al., 2012, 2016, 2018), seemed to work coherently when detecting burned areas as errors of omission appeared when low backscatter changes were observed over burned areas while error of commissions appeared due to fire unrelated backscatter variations over unburned areas. These trends were reflected by the MAC values for OE and CE classes which were close to those observed for unburned and respectively burned areas suggesting a correct estimation of the covariance matrices by taking advantage of the *a priori* information from stable areas (i.e., likely unburned pixels). Comparing backscatter variability over burned and unburned classes one may notice notably smaller MAC values over the later which also suggests a properly functioning of the anomaly detector according to the input data. To test the correct delineation of stable areas (i.e., background), a t-test was used to analyse the statistical difference between the inverted covariance matrices (used by RXD) obtained using hotspots and those obtained using the BA validation perimeters from optical data (Section 3.4). The analysis showed no statistical difference (p-values > 0.05) between the two methods demonstrating that hotspots may be reliably used to identify likely burned and unburned pixels as a preliminary source of burned area.

The use of ancillary information from thermal anomalies (hotspots) allowed for attributing anomalous changes of SAR backscatter data as BA though a locally derived knowledge extraction. Hence, burned pixels were extracted without the need for relying on fixed thresholds

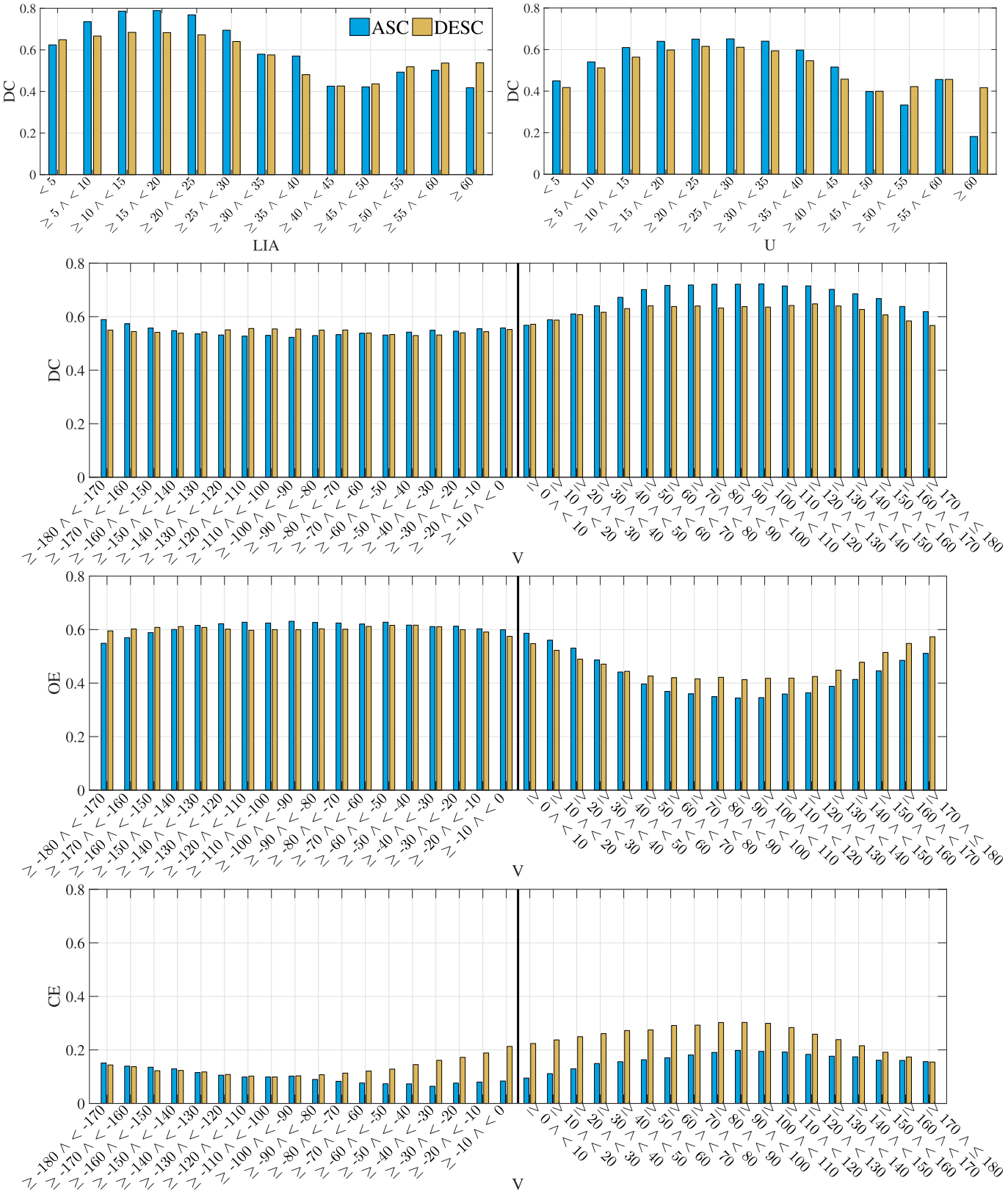

Fig. 10. Dice coefficient (DC) by local incidence angle (LIA) and local slope (U) groups. For sloped areas (U ≥ 5°) the DC, commission (CE) and omission errors (OE) are shown as a function of slope orientation (V) with respect to the Sentinel-1 viewing geometry. Negative V values show slopes oriented away the sensor while positive V values show slopes oriented toward the sensor. The BA metrics are shown for six tiles where both ascending (ASC) and descending (DESC) passes were available (i.e., 10SEH, 10UEC, 29TNE, 29TNG, 30SVG and 30TYK).

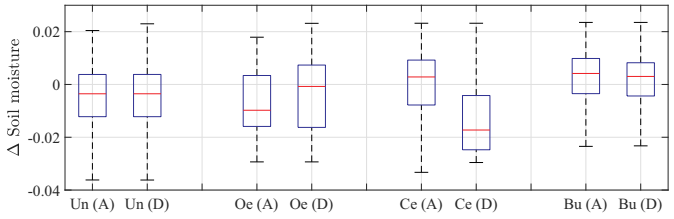

Fig. 11. Temporal variations of soil moisture (SM) from Soil Moisture Active Passive (SMAP) mission for pre- and post-fire dates ($\Delta_{SM} = SM_{pre} - SM_{post}$), in tile 30SVG. Ascending (A) and descending (D) passes are analyzed separately. Pixels are grouped by classes of unburned (Un) and burned (Bu). Pixels from areas affected by commission (Ce) and omission errors (Oe) are also shown. The red line indicates median value, and top and bottom box edges indicate the 75th and respectively the 25th percentiles. Outliers are not shown to improve graph discernibility.

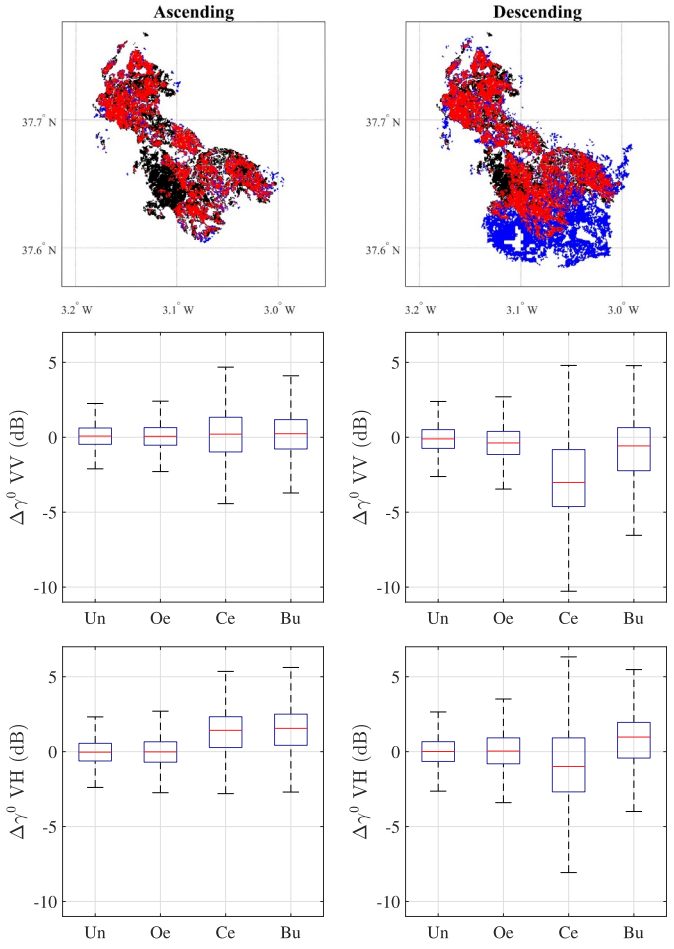

Fig. 12. Burned area from ascending (left column) and descending (right column) passes in tile 30SVG: red – burned (Bu), white – unburned (Un), black – omission errors (Oe) and blue – commission errors (Ce). VV and VH backscatter coefficient variation ($\Delta\gamma^0 = pre_{fire} - post_{fire}$) is also shown for each pass.

on the SAR signal, which may depend not only on the land cover type, but also on backscatter variations due to spatially variable influencing factors (e.g., soil and vegetation moisture) that are difficult to model. Temporal decorrelation between hotspots (i.e., fire date) and the date at which radar backscatter changes were detected (Belenguer-Plomer et al., 2018b) was observed over most tiles. One should notice that temporal decorrelation is not specific to burned area nor the C-band frequency as similar effects were observed for L-band HV polarization over areas affected by deforestation (Watanabe et al., 2018). Therefore, temporal studies using SAR-based change detection techniques must devise methods to reduce or account for such effects (see the proposed approach in the Stage 3).

The use of a non-parametric classifier was essential to cope the temporal lack of hotspots due to persistent cloud cover or small fire size (i.e., not detected by thermal sensors). Parametrising random forests classifier (RF) for BA classification may prove complex as almost an infinite combinations of parameter settings are possible. Ramo & Chuvieco (2017) proposed using 600 trees and a stratified training, where 10% of training data were burned pixels and the rest not burned, for the classification of MODIS images in burned and unburned classes. Such a setting was tested during algorithm development but the results were not as accurate as expected. Therefore, the RF set-up was customized based on empirical observations. The substantial differences in RF parametrization settings were mainly caused by the algorithm design, since it is building specific RF models for each land cover type and detection period. Hence, it does not have to cope with widely varying land cover and burn conditions as the work of Ramo & Chuvieco (2017) which used one uniquely trained model worldwide.

5.2. Comparison with global products

Over most validation areas, the accuracy of the proposed algorithm was higher when compared to the MCD64A1 Version 6 product (Giglio et al., 2018). The mean DC value over all studied locations was 0.13 higher for the Sentinel-1 BA detections (i.e., 28% higher). The DC values of Sentinel-1 detections per tiles were statistically higher than those of MCD64A1 (paired t-test p-value of 0.024). In addition, the variability of Sentinel-1 BA detection accuracy was considerably lower when compared to the MCD64A1 product. The mean values for OE and CE over all tiles were also lower for the Sentinel-1 detections.

The analysis showed that for 13 tiles (72% of the studied areas) the Sentinel-1 BA detections had higher DC scores than the MCD64A1 product. For one tile, 33NUF, the difference in accuracy (DC) of the two products is 0.5. The very low accuracy (DC 0.02) observed over this tile for the MCD64A1 product is difficult to explain with the data at hand, hence the tile was considered an outlier. For five tiles (i.e., 18NXG, 30TYK, 33NTG, 33NUG, and 49MHT) the improvement of the Sentinel-1 product was substantial with DC increasing on average by 144% when compared to the MCD64A1 product. The large difference in DC scores was mainly caused by the high OE (0.72 to 0.94) in the MCD64A1 product. Detection of small burned areas (< 120 ha) is problematic using MODIS data due to the coarse sensor resolution (Giglio et al., 2009). To evaluate if reduced spatial resolution of MODIS was the reason behind MCD64A1 product poor performance, the percentage of BA from fire scars below 120 ha was computed based on the reference datasets. In tiles 33NUG, 33NTG, and 49MHT fires below 120 ha constituted 85%, 53% and respectively 48% of the total BA suggesting that the lower performance may be related to the coarser MODIS spatial resolution. Therefore, these results suggest that improvements in BA detection accuracy may be possible not only in areas with frequent cloud cover. However, for tiles 18NXG and 30TYK small fires (< 120 ha) constituted only 34% and respectively 25% of the total BA indicating that fire size may not be the only factor influencing detection accuracy when using coarse resolution sensors.

For five tiles (i.e., 29TNE, 30SVG, 36NXP, 48VWL and 50JML) the MCD64A1 product showed higher DC scores when compared to the Sentinel-1 based detections. The mean difference for the four first tiles was only 0.13. However, for tile 50JML this difference was higher, with the MCD64A1 product being markedly more accurate (DC 0.41 vs. 0.21). It seems such large differences were related to the conditions encountered over the Australian grasslands, where backscatter variations recorded from pre- to post-fire periods were low, hindering the detection algorithm. By land cover class, the results indicate that a radar-based BA mapping algorithm may provide BA products with better or similar accuracies when compared to available global products, except for grasslands. The most significant difference in accuracy

was observed over grasslands, where the MCD64A1 was more accurate than the Sentinel-1 based BA (DC 0.45 vs. 0.28). Conversely, over forests Sentinel-1 derived BA was more accurate (DC 0.64 vs. 0.49).

5.3. Factors influencing BA accuracy

Temporal variation of pre- and post-fire VH and VV backscatter coefficient over pixels affected by CE and OE were similar to those observed over burned and respectively unburned pixels. Following, the main factors affecting burned area classification were discussed.

5.3.1. Environmental conditions

CE may only be related to factors that modify the scattering proprieties in a similar manner to fires (e.g., soil moisture variations) when backscatter changes are concentrated in a reduced part of the image (anomalous changes), since the RXD may identify such variations as spatial anomalies and consequently the algorithm may misclassify them as BA. For instance, unrelated fire backscatter variations which did not affect the entire image occurred over tile 30SVG, where the highest difference between commission errors for ascending (0.16) and descending (0.46) passes were observed. For this tile, soil moisture variations over CE pixels varied notably between ascending and descending passes. For the descending pass, post-fire soil moisture was on average 0.014 ± 1.18e-04 m^3/m^3 higher when compared to pre-fire soil moisture, while for the ascending pass the increment was marginal (6.2e-04 m^3/m^3). Consequently, over pixels affected by CE, an average increase of 2.8 ± 0.029 dB for VV polarization and 1.0 ± 0.027 dB for the VH polarization was recorded from pre- to post-fire date for the descending acquisitions. The differentiated increase by polarization confirmed the larger influence of the soil surface properties on the VV polarization when compared to the VH polarization as noted previously by the other authors (Freeman & Durden, 1998; Yamaguchi et al., 2005; Van Zyl et al., 2011). The backscatter coefficient change generated by variations in soil moisture was incorrectly mapped as burned since: (i) the algorithm does not account for the sign of the backscatter change; and (ii) the image part affected by rainfall was located close to hotspots (areas bordering the fire perimeter). This suggests that algorithm improvements may further mitigate commission errors related to soil moisture variations by considering the backscatter change direction. Notice that, tile 30SVG was an exception as, at this location, a major part (67.6%) of the CE were concentrated in a large enough area (3420 ha) to extract useful information from the coarse pixel spacing SMAP product. The influence of soil moisture on BA accuracy was inconclusive for the rest of the tiles, most probably due to the coarse pixel spacing of the SMAP product (9 km). The use of higher spatial resolution soil moisture products such as the Copernicus Surface Soil Moisture (SSM), a Sentinel-1 based product with 1 km of pixel spacing (Bauer-Marschallinger et al., 2018), shall be investigated once they become available at global level. Further, as global products of harvest, defoliation, floods or logging at enough detailed pixel spacing, when compared to Sentinel-1 spatial resolution, are not available and precipitation products based on extrapolation of data from rain gauges have a much coarser pixel spacing (0.5°) and own errors (Hu et al., 2018), it was not possible to identify all the commission errors sources and filter them out.

5.3.2. Fire impact

Conversely, pixels affected by OE may have been the result of the effects of different variables which attenuated the vegetation combustion effects on the C-band backscatter coefficient. Fire severity, the degree of organic matter loss due to fire combustion (Keeley, 2009), constrains the temporal backscatter variation between pre- and post-fire (Tanase et al., 2010b, 2014). The dNBR mean values over the pixels affected by omission errors were 22.73% lower when compared to the dNBR values observed for correctly detected burned pixels. Notice that the dNBR index is widely used to detect BA and estimate fire severity over a range of biomes (Escuin et al., 2008; Loboda et al., 2007; Van Wagtendonk et al., 2004; Tanase et al., 2011) and that high fire severity implies a more significant reduction of vegetated scattering elements due to combustion.

5.3.3. Topography

Topography also affected the BA accuracy, with a tendency of increased burned areas omission being observed for the pixels oriented away from the sensor most likely due to the existence of shadowed regions (Tanase et al., 2010a, 2009). Conversely, for the pixels oriented towards the sensor the commission errors increased since soil proprieties had a higher influence on radar scattering. Since the OE due to topographic effects were higher when compared to the CE, BA accuracy was improved by joining detections from different relative orbits when available (see Subsubsection 5.3.5).

5.3.4. Land cover type

The variables mentioned above affect the scattering processes over burned and unburned areas differently depending of the land cover class observed and translated into variable map accuracies. Lower BA accuracies were found over grasslands as the scattering elements characteristic for this vegetation type interact to a lesser extent with the C-band waves when compared to the scattering elements encountered in shrubs and forests (e.g., stems, branches). However, the most important factor affecting the algorithm sensitivity to fire in grasslands seemed to be related to fire timing. In areas characterized by long intervals (months) between grass curing and fire events the algorithm encountered difficulties as the cured (i.e., dry) grass has low scattering properties being mostly transparent to the radar waves (Menges et al., 2004). Therefore, grass consumption by fire results in small or nil VV and VH backscatter changes from vegetation consumption which hinders BA detection. This observation seemed supported by the lower temporal variation of the backscatter coefficient over burned when compared unburned grasslands. Conversely, forest and shrubs, besides containing scattering elements more susceptible to interact to C-band radar waves, are not affected by curing to the same extent (i.e., some water needs to be retained to ensure plant survival). Thus, vegetation consumption by fire results in a noticeable scattering decrease which is detected by the algorithm, although sometimes a temporal gap between fire and detection was observed (temporal decorrelation) as discussed in Belenguer-Plomer et al. (2018b).

5.3.5. Ancillary information and SAR data availability

The use of hotspots was essential given that only two backscatter channels were available (VV and VH polarizations). Without hotspots, differentiation of burned areas from other land changes (e.g., floods, logging, harvest, vegetation disturbance due to pests, drought) that modulate the backscatter coefficient in a similar fashion was difficult as also noted by Huang & Siegert (2006). Lower BA detection accuracies were found in pixels located far (outside IAhs) when compared to pixels located in close proximity (within 750 m) of hotpots events (see supplementary data). According to the reference data, only a 15.3% of burned pixels were not located within IAhs allowing for BA detection rates comparable or better than those of currently available global products.

Joining detections from different relative orbits (from ascending and descending passes) increased the detected burned area. Inherently, the availability of several orbits covering the same area resulted in reduced OE which is particularly true when different viewing geometries were used over areas with steep topography. Conversely the CE increased as wrongly detected areas are also joined in post-processing (Stage 5 of the algorithm). Despite the increased CEs, the use of both Sentinel-1 passes generally improved the BA accuracy. It should be noted that consistent dual pass (ascending and descending) acquisitions are currently available only over Europe and North America. The analysis suggested that differences in BA accuracy between ascending

and descending passes were mainly caused by the interaction between the viewing geometry and the local topography as explained in Subsection 4.3, with the highest accuracies being achieved over areas oriented towards the sensor. Using images acquired in a single pass may result in increased omission errors particularly in regions with accentuated topography. These results confirm previous findings that highlight the effect of topography on burned area detection and fire impact estimation (Gimeno & San-Miguel-Ayanz, 2004; Huang & Siegert, 2006; Tanase et al., 2010b). Further investigations of topographic effects reduction are needed as, under the current observation scenario, for most of the Earth surface Sentinel-1 data are consistently acquired in only one pass (i.e., ascending or descending).

The accuracy of the Sentinel-1 product was also assessed as a function of the number of SAR images available during the detection period as well as the number of days between consecutive acquisitions. The BA was detected regardless of the image number or their temporal distance, thus coping with the variable acquisition strategy (temporal frequency) of the Sentinel-1 mission over different regions. The main temporal factor which limited the algorithm accuracy was the post-fire vegetation regrowth cycle. Where image acquisitions were more frequent, when compared to vegetation regrowth cycles, the algorithm detected the changes in backscatter coefficient generated by fires and labelled them as BA. However, the relationship between BA detection accuracy (DC) and the number of images used and their acquisition frequency (day difference of consecutive images) per tiles was weak (0.32 and respectively 0.38 Pearson's correlation coefficient) since additional factors affected the algorithm accuracy (i.e., topography and fire unrelated changes). Thus, it was concluded that current Sentinel-1 temporal frequencies might be sufficient for global retrieval. Nevertheless, the relatively small number of test samples may have obscured some effects. In addition, the relationship between Sentinel-1 acquisition frequency and the detection accuracy may vary with the land cover type (different post-fire regrowth cycle).

5.4. Comparison with previous Sentinel-1 based approaches

Previous studies based on Sentinel-1 data for BA detection were carried out only at local to regional scales. However, C-band backscatter from fire affected areas varies with the local conditions. Therefore, locally trained algorithms are difficult to transfer to other regions. Engelbrecht et al. (2017) used empirical thresholds to detect BA in South Africa achieving OE and CE of 0.29 and 0.48, respectively. Depending on area, the proposed algorithm may achieve similar or better accuracies. Lohberger et al. (2018) used an object-based image analysis approach to detect BA in Indonesia. However, since only information on the overall accuracy was provided comparisons were difficult. Finally, Verhegghen et al. (2016) tested the most suitable thresholds when separating burned from unburned pixels in the Congo basin, but did not provide accuracy metrics of their detected BA. Nevertheless, since such studies relied on algorithms heavily optimized over local to regional scales, comparisons with the proposed algorithm are of little relevance.

6. Conclusions

This paper introduced an automated and cloud cover insensitive algorithm for BA detection using Sentinel-1 dual-polarized backscatter images. Hotspots from active fires and land cover data were used as ancillary information when attributing anomalous backscatter changes to burned and unburned classes. The algorithm was validated at 18 locations (100 × 100 km tiles) covering over 21 million hectares worldwide. Algorithm accuracy was assessed using reference burn perimeters derived from optical sensors (Landsat-8 and Sentinel-2). The agreement between the Sentinel-1 algorithm and the reference perimeters was compared with that of the most widely used global BA product, the MCD64A1 Version 6. Over all tiles, the mean OE and CE for BA were 0.43 and 0.37, respectively. The mean DC was 0.59. When compared with the MCD64A1, the proposed algorithm improved burned area detection (DC) by 28% (from 0.46 to 0.59) over the analysed tiles. Such improvements in accuracy were mainly related to reduced OE, a useful trait demonstrating that Sentinel-1 data may be a key source of information when optical data based products have information gaps due to persistent cloud cover.

According to our analysis, strong topography conditioned the BA accuracy with slopes oriented away from the sensor being subject to higher errors. Such effects were reduced by combining detections from different relative orbits. Likewise, it was observed that a reduced fire severity translated into increased omission errors. On the other hand, commission errors seemed to correlate with fire unrelated changes affecting the scattering processes. Furthermore, scattering from burned areas was directly influenced by vegetation type with higher accuracies being observed over forested areas (DC 0.64) and lower over grasslands (DC 0.28) which were attributed to the difficulty in tracking changes of cured vegetation using the C-band data. The main advantages of the proposed algorithm were related to: (i) self-adapting to local scattering conditions without the need for *a priori* information of the observed area or the use of fixed thresholds; and (ii) ability to detect BA during periods with no thermal anomalies. On the other hand, the main limitations were related to the: (i) misclassification of fire unrelated changes; (ii) positive relationship between accuracy and hotspots availability; and (iii) accuracy dependence on variables affecting radar scattering processes (e.g., ecosystem type, topography). To reduce such limitations, further improvements shall be investigated.

Acknowledgements

This work has been financed by the European Space Agency through the Phase 2 of the Fire_cci (Climate Change Initiative) project (Contract 4000115006/15/I-NB) and by the Spanish Ministry of Science, Innovation and Universities through a FPU doctoral fellowship (FPU16/01645). We acknowledge the use of data from LANCE FIRMS operated by the NASA GSFC Earth Science Data and Information System (ESDIS). We also acknowledge Dr. Thierry Koleck and Dr. Stephane Mermoz for kindly providing the code for Sentinel-1 data pre-processing and the comments and suggestions of several anonymous reviewers which helped in improving the original manuscript.

Appendix A. Supplementary data

Supplementary data to this article can be found online at https://doi.org/10.1016/j.rse.2019.111345.

References

Alonso-Canas, I., Chuvieco, E., 2015. Global burned area mapping from ENVISAT-MERIS and MODIS active fire data. Remote Sens. Environ. 163, 140–152.
Andela, N., Morton, D., Giglio, L., Chen, Y., Van Der Werf, G., Kasibhatla, P., DeFries, R., Collatz, G., Hantson, S., Kloster, S., et al., 2017. A human-driven decline in global burned area. Science 356, 1356–1362.
Andreae, M.O., Merlet, P., 2001. Emission of trace gases and aerosols from biomass burning. Glob. Biogeochem. Cycles 15, 955–966.
Antikidis, E., Arino, O., Arnaud, A., Laur, H., 1998. ERS SAR coherence & ATSR hot spots: a synergy for mapping deforested areas. The special case of the 1997 fire event in Indonesia. Eur. Space Agency-Publ.-ESA SP 441, 355–360.
Aponte, C., de Groot, W.J., Wotton, B.M., 2016. Forest fires and climate change: causes, consequences and management options. Int. J. Wildland Fire 25, i–ii.
Banerjee, A., Burlina, P., Diehl, C., 2006. A support vector method for anomaly detection in hyperspectral imagery. IEEE Trans. Geosci. Remote Sens. 44, 2282–2291.
Bastarrika, A., Chuvieco, E., Martín, M.P., 2011. Mapping burned areas from Landsat TM/ETM+ data with a two-phase algorithm: balancing omission and commission errors. Remote Sens. Environ. 115, 1003–1012.
Bauer-Marschallinger, B., Freeman, V., Cao, S., Paulik, C., Schaufler, S., Stachl, T., Modanesi, S., Massari, C., Ciabatta, L., Brocca, L., et al., 2018. Toward global soil moisture monitoring with Sentinel-1: harnessing assets and overcoming obstacles. IEEE Transactions on Geoscience and Remote Sensing 1–20.
Belenguer-Plomer, M.A., Tanase, M.A., Fernandez-Carrillo, A., Chuvieco, E., 2018a. Insights into burned areas detection from Sentinel-1 data and locally adaptive

algorithms. In: Active and Passive Microwave Remote Sensing for Environmental Monitoring II. 10788. International Society for Optics and Photonics, pp. 107880G.
Belenguer-Plomer, M.A., Tanase, M.A., Fernandez-Carrillo, A., Chuvieco, E., 2018b. Temporal backscattering coefficient decorrelation in burned areas. In: Active and Passive Microwave Remote Sensing for Environmental Monitoring II. 10788. International Society for Optics and Photonics, pp. 107880T.
Belgiu, M., Drăguţ, L., 2016. Random forest in remote sensing: a review of applications and future directions. ISPRS J. Photogramm. Remote Sens. 114, 24–31.
Bojinski, S., Verstraete, M., Peterson, T.C., Richter, C., Simmons, A., Zemp, M., 2014. The concept of essential climate variables in support of climate research, applications, and policy. Bull. Am. Meteorol. Soc. 95, 1431–1443.
Bond, W.J., Woodward, F.I., Midgley, G.F., 2005. The global distribution of ecosystems in a world without fire. New Phytol. 165, 525–538.
Boschetti, L., Flasse, S.P., Brivio, P.A., 2004. Analysis of the conflict between omission and commission in low spatial resolution dichotomic thematic products: the Pareto boundary. Remote Sens. Environ. 91, 280–292.
Boschetti, L., Roy, D.P., Justice, C.O., Giglio, L., 2010. Global assessment of the temporal reporting accuracy and precision of the MODIS burned area product. Int. J. Wildland Fire 19, 705–709.
Bourgeau-Chavez, L., Harrell, P., Kasischke, E., French, N., 1997. The detection and mapping of Alaskan wildfires using a spaceborne imaging radar system. Int. J. Remote Sens. 18, 355–373.
Bourgeau-Chavez, L., Kasischke, E., Brunzell, S., Mudd, J., Tukman, M., 2002. Mapping fire scars in global boreal forests using imaging radar data. Int. J. Remote Sens. 23, 4211–4234.
Bowman, D.M., Balch, J.K., Artaxo, P., Bond, W.J., Carlson, J.M., Cochrane, M.A., D'Antonio, C.M., DeFries, R.S., Doyle, J.C., Harrison, S.P., et al., 2009. Fire in the Earth system. Science 324, 481–484.
Bradley, A.V., Tansey, K., Chuvieco, E., 2012. The ESA climate change initiative: merging burned area estimates for the fire essential climate variable. In: 2012 IEEE International Geoscience and Remote Sensing Symposium (IGARSS). IEEE, pp. 7153–7156.
Breiman, L., 2001. Random forests. Mach. Learn. 45, 5–32.
Chan, S., 2016. Enhanced Level 3 Passive Soil Moisture Product Specification Document. Jet Propulsion Lab., California Inst. Technol., Pasadena, CA, USA.
Chan, S., Bindlish, R., O'Neill, P., Jackson, T., Njoku, E., Dunbar, S., Chaubell, J., Piepmeier, J., Yueh, S., Entekhabi, D., et al., 2018. Development and assessment of the SMAP enhanced passive soil moisture product. Remote Sens. Environ. 204, 931–941.
Chawla, N.V., Bowyer, K.W., Hall, L.O., Kegelmeyer, W.P., 2002. SMOTE: Synthetic Minority Over-sampling Technique. J. Artif. Intell. Res. 16, 321–357.
Chen, C., Liaw, A., Breiman, L., 2004. Using Random Forest to Learn Imbalanced Data. 110 University of California, Berkeley.
Chen, Q., Zeng, J., Cui, C., Li, Z., Chen, K.-S., Bai, X., Xu, J., 2018. Soil moisture retrieval from SMAP: a validation and error analysis study using ground-based observations over the little Washita watershed. IEEE Trans. Geosci. Remote Sens. 56, 1394–1408.
Chuvieco, E., Lizundia-Loiola, J., Pettinari, M.L., Ramo, R., Padilla, M., Mouillot, F., Laurent, P., Storm, T., Heil, A., Plummer, S., 2018. Generation and analysis of a new global burned area product based on MODIS 250 m reflectance bands and thermal anomalies. Earth Syst. Sci. Data Discuss. 512, 1–24.
Chuvieco, E., Yue, C., Heil, A., Mouillot, F., Alonso-Canas, I., Padilla, M., Pereira, J.M., Oom, D., Tansey, K., 2016. A new global burned area product for climate assessment of fire impacts. Glob. Ecol. Biogeogr. 25, 619–629.
Collins, L., Griffioen, P., Newell, G., Mellor, A., 2018. The utility of random forests for wildfire severity mapping. Remote Sens. Environ. 216, 374–384.
Dabbiru, L., Aanstoos, J.V., Mahrooghy, M., Li, W., Shanker, A., Younan, N.H., 2012. Levee anomaly detection using polarimetric synthetic aperture radar data. In: 2012 IEEE International Geoscience and Remote Sensing Symposium (IGARSS). IEEE, pp. 5113–5116.
Dabbiru, L., Aanstoos, J.V., Younan, N.H., 2016. Earthen levee slide detection via automated analysis of synthetic aperture radar imagery. Landslides 13, 643–652.
Dabbiru, L., Aanstoos, J.V., Ball, J.E., Younan, N.H., 2018. Machine learning framework for mapping of Mississippi River levees and damage assessment using Terrasar-X data. In: IGARSS 2018-2018 IEEE International Geoscience and Remote Sensing Symposium. IEEE, pp. 5855–5858.
Di Gregorio, A., 2005. Land Cover Classification System: Classification Concepts and User manual. United Nations Food and Agriculture Organization.
Du, P., Samat, A., Waske, B., Liu, S., Li, Z., 2015. Random forest and rotation forest for fully polarized SAR image classification using polarimetric and spatial features. ISPRS J. Photogramm. Remote Sens. 105, 38–53.
Engelbrecht, J., Theron, A., Vhengani, L., Kemp, J., 2017. A simple normalized difference approach to burnt area mapping using multi-polarisation C-Band SAR. Remote Sens. 9, 764.
Escuin, S., Navarro, R., Fernandez, P., 2008. Fire severity assessment by using NBR (Normalized Burn Ratio) and NDVI (Normalized Difference Vegetation Index) derived from LANDSAT TM/ETM images. Int. J. Remote Sens. 29, 1053–1073.
Eva, H., Lambin, E.F., 1998. Remote sensing of biomass burning in tropical regions: sampling issues and multisensor approach. Remote Sens. Environ. 64, 292–315.
Fernandez-Carrillo, A., Belenguer-Plomer, M., Chuvieco, E., Tanase, M., 2018. Effects of sample size on burned areas accuracy estimates in the Amazon Basin. In: Earth Resources and Environmental Remote Sensing/GIS Applications IX. 10790. International Society for Optics and Photonics, pp. 107901S.
Flannigan, M.D., Amiro, B.D., Logan, K.A., Stocks, B., Wotton, B., 2006. Forest fires and climate change in the 21st century. Mitig. Adapt. Strateg. Glob. Chang. 11, 847–859.
Flannigan, M.D., Krawchuk, M.A., de Groot, W.J., Wotton, B.M., Gowman, L.M., 2009. Implications of changing climate for global wildland fire. Int. J. Wildland Fire 18, 483–507.
Freeman, A., Durden, S.L., 1998. A three-component scattering model for polarimetric SAR data. IEEE Trans. Geosci. Remote Sens. 36, 963–973.
French, N.H., Bourgeau-Chavez, L.L., Wang, Y., Kasischke, E.S., 1999. Initial observations of Radarsat imagery at fire-disturbed sites in interior Alaska. Remote Sens. Environ. 68, 89–94.
Frey, O., Santoro, M., Werner, C.L., Wegmuller, U., 2013. DEM-based SAR pixel-area estimation for enhanced geocoding refinement and radiometric normalization. IEEE Geosci. Remote Sens. Lett. 10, 48–52.
García, M.L., Caselles, V., 1991. Mapping burns and natural reforestation using Thematic Mapper data. Geocarto Int. 6, 31–37.
Giglio, L., Loboda, T., Roy, D.P., Quayle, B., Justice, C.O., 2009. An active-fire based burned area mapping algorithm for the MODIS sensor. Remote Sens. Environ. 113, 408–420.
Giglio, L., Boschetti, L., Roy, D.P., Humber, M.L., Justice, C.O., 2018. The collection 6 MODIS burned area mapping algorithm and product. Remote Sens. Environ. 217, 72–85.
Giglio, L., Descloitres, J., Justice, C.O., Kaufman, Y.J., 2003. An enhanced contextual fire detection algorithm for MODIS. Remote Sens. Environ. 87, 273–282.
Gimeno, M., San-Miguel-Ayanz, J., Schmuck, G., 2004. Identification of burnt areas in Mediterranean forest environments from ERS-2 SAR time series. Int. J. Remote Sens. 25, 4873–4888.
Gimeno, M., San-Miguel, J., Barbosa, P., Schmuck, G., 2002. Using ERS-SAR images for burnt area mapping in Mediterranean landscapes. In: Viegas, T. (Ed.), Forest Fire Research & Wildland Fire Safety. 90 Millpress, Rotterdam.
Gimeno, M., San-Miguel-Ayanz, J., 2004. Evaluation of RADARSAT-1 data for identification of burnt areas in Southern Europe. Remote Sens. Environ. 92, 370–375.
Gislason, P.O., Benediktsson, J.A., Sveinsson, J.R., 2006. Random forests for land cover classification. Pattern Recogn. Lett. 27, 294–300.
Hansen, M.C., Potapov, P.V., Moore, R., Hancher, M., Turubanova, S., Tyukavina, A., Thau, D., Stehman, S., Goetz, S., Loveland, T., et al., 2013. High-resolution global maps of 21st-century forest cover change. Science 342, 850–853.
Hoffmann, W.A., Schroeder, W., Jackson, R.B., 2002. Positive feedbacks of fire, climate, and vegetation and the conversion of tropical savanna. Geophys. Res. Lett. 29 9–1.
Hollmann, R., Merchant, C.J., Saunders, R., Downy, C., Buchwitz, M., Cazenave, A., Chuvieco, E., Defourny, P., de Leeuw, G., Forsberg, R., et al., 2013. The ESA climate change initiative: satellite data records for essential climate variables. Bull. Am. Meteorol. Soc. 94, 1541–1552.
Hu, Z., Zhou, Q., Chen, X., Li, J., Li, Q., Chen, D., Liu, W., Yin, G., 2018. Evaluation of three global gridded precipitation data sets in central Asia based on rain gauge observations. Int. J. Climatol. 38, 3475–3493.
Huang, S., Siegert, F., 2006. Backscatter change on fire scars in Siberian boreal forests in ENVISAT ASAR wide-swath images. IEEE Geosci. Remote Sens. Lett. 3, 154–158.
Humber, M.L., Boschetti, L., Giglio, L., Justice, C.O., 2018. Spatial and temporal intercomparison of four global burned area products. Int. J. Digital Earth 1–25.
Imperatore, P., Azar, R., Calo, F., Stroppiana, D., Brivio, P.A., Lanari, R., Pepe, A., 2017. Effect of the vegetation fire on backscattering: an investigation based on Sentinel-1 observations. IEEE J. Sel. Top. Appl. Earth Obs. Remote Sens. 10, 4478–4492.
Inglada, J., Christophe, E., 2009. The Orfeo Toolbox remote sensing image processing software. In: Geoscience and Remote Sensing Symposium, 2009 IEEE International, IGARSS 2009. 4. IEEE, pp. IV–733.
Kalogirou, V., Ferrazzoli, P., Della Vecchia, A., Foumelis, M., 2014. On the SAR backscatter of burned forests: a model-based study in C-band, over burned pine canopies. IEEE Trans. Geosci. Remote Sens. 52, 6205–6215.
Kasischke, E.S., Bourgeau-Chavez, L.L., French, N.H., 1994. Observations of variations in ERS-1 SAR image intensity associated with forest fires in Alaska. IEEE Trans. Geosci. Remote Sens. 32, 206–210.
Keeley, J.E., 2009. Fire intensity, fire severity and burn severity: a brief review and suggested usage. Int. J. Wildland Fire 18, 116–126.
Key, C., Benson, N., 2006. Ground measure of severity, the Composite Burn Index; and Remote sensing of severity, the Normalized Burn Ratio. chapter Landscape assessment (LA): Sampling and analysis methods In: RMRS-GTR-164, G.T.R. (Ed.), FIREMON: Fire Effects Monitoring and Inventory System. USDA Forest Service, Rocky Mountain Research Station, Ogden, pp. 1–51.
Kirches, G., Brockmann, C., Boettcher, M., Peters, M., Bontemps, S., Lamarche, C., Schlerf, M., Santoro, M., Defourny, P., 2014. Land Cover CCI-Product User Guide-Version 2. In: ESA Public Document CCI-LC-PUG, pp. 4.
Kloster, S., Mahowald, N., Randerson, J., Lawrence, P., 2012. The impacts of climate, land use, and demography on fires during the 21st century simulated by CLM-CN. Biogeosciences 9, 509–525.
Knorr, W., Jiang, L., Arneth, A., 2016. Climate, CO 2 and human population impacts on global wildfire emissions. Biogeosciences 13, 267–282.
Krawchuk, M.A., Moritz, M.A., Parisien, M.-A., Van Dorn, J., Hayhoe, K., 2009. Global pyrogeography: the current and future distribution of wildfire. PloS one 4, e5102.
Kurum, M., 2015. C-band SAR backscatter evaluation of 2008 Gallipoli forest fire. IEEE Geosci. Remote Sens. Lett. 12, 1091–1095.
Kwon, H., Nasrabadi, N.M., 2005. Kernel RX-algorithm: a nonlinear anomaly detector for hyperspectral imagery. IEEE Trans. Geosci. Remote Sens. 43, 388–397.
Lacava, T., Coviello, I., Faruolo, M., Mazzeo, G., Pergola, N., Tramutoli, V., 2013. A multitemporal investigation of AMSR-E C-band radio-frequency interference. IEEE Trans. Geosci. Remote Sens. 51, 2007–2015.
Langenfelds, R., Francey, R., Pak, B., Steele, L., Lloyd, J., Trudinger, C., Allison, C., 2002. Interannual growth rate variations of atmospheric CO2 and its δ13C, H2, CH4, and CO between 1992 and 1999 linked to biomass burning. Glob. Biogeochem. Cycles 16 21–1.
Lavorel, S., Flannigan, M.D., Lambin, E.F., Scholes, M.C., 2007. Vulnerability of land

systems to fire: interactions among humans, climate, the atmosphere, and ecosystems. Mitig. Adapt. Strateg. Glob. Chang. 12, 33–53.
Li, L., Njoku, E.G., Im, E., Chang, P.S., Germain, K.S., 2004. A preliminary survey of radio-frequency interference over the US in Aqua AMSR-E data. IEEE Trans. Geosci. Remote Sens. 42, 380–390.
Loboda, T., O'neal, K., Csiszar, I., 2007. Regionally adaptable dNBR-based algorithm for burned area mapping from MODIS data. Remote Sens. Environ. 109, 429–442.
Lohberger, S., Stängel, M., Atwood, E.C., Siegert, F., 2018. Spatial evaluation of Indonesia's 2015 fire-affected area and estimated carbon emissions using Sentinel-1. Glob. Chang. Biol. 24, 644–654.
Meddens, A.J., Kolden, C.A., Lutz, J.A., 2016. Detecting unburned areas within wildfire perimeters using Landsat and ancillary data across the northwestern United States. Remote Sens. Environ. 186, 275–285.
Menges, C., Bartolo, R., Bell, D., Hill, G.E., 2004. The effect of savanna fires on SAR backscatter in northern Australia. Int. J. Remote Sens. 25, 4857–4871.
Mouillot, F., Schultz, M.G., Yue, C., Cadule, P., Tansey, K., Ciais, P., Chuvieco, E., 2014. Ten years of global burned area products from spaceborne remote sensing–a review: analysis of user needs and recommendations for future developments. Int. J. Appl. Earth Obs. Geoinf. 26, 64–79.
Njoku, E.G., Ashcroft, P., Chan, T.K., Li, L., 2005. Global survey and statistics of radio-frequency interference in AMSR-E land observations. IEEE Trans. Geosci. Remote Sens. 43, 938–947.
Padilla, M., Stehman, S.V., Chuvieco, E., 2014. Validation of the 2008 MODIS-MCD45 global burned area product using stratified random sampling. Remote Sens. Environ. 144, 187–196.
Padilla, M., Stehman, S.V., Ramo, R., Corti, D., Hantson, S., Oliva, P., Alonso-Canas, I., Bradley, A.V., Tansey, K., Mota, B., et al., 2015. Comparing the accuracies of remote sensing global burned area products using stratified random sampling and estimation. Remote Sens. Environ. 160, 114–121.
Padilla, M., Olofsson, P., Stehman, S.V., Tansey, K., Chuvieco, E., 2017. Stratification and sample allocation for reference burned area data. Remote Sens. Environ. 203, 240–255.
Pal, M., 2005. Random forest classifier for remote sensing classification. Int. J. Remote Sens. 26, 217–222.
Pausas, J.G., Paula, S., 2012. Fuel shapes the fire-climate relationship: evidence from Mediterranean ecosystems. Glob. Ecol. Biogeogr. 21, 1074–1082.
Pazzani, M., Merz, C., Murphy, P., Ali, K., Hume, T., Brunk, C., 1994. Reducing misclassification costs. In: Machine Learning Proceedings 1994, pp. 217–225.
Plummer, S., Arino, O., Simon, M., Steffen, W., 2006. Establishing a earth observation product service for the terrestrial carbon community: the GLOBCARBON initiative. Mitig. Adapt. Strateg. Glob. Chang. 11, 97–111.
Plummer, S., Lecomte, P., Doherty, M., 2017. The ESA Climate Change Initiative (CCI): a European contribution to the generation of the Global Climate Observing System. Remote Sens. Environ. 203, 2–8.
Polychronaki, A., Gitas, I.Z., Veraverbeke, S., Debien, A., 2013. Evaluation of ALOS PALSAR imagery for burned area mapping in Greece using object-based classification. Remote Sens. 5, 5680–5701.
Poulter, B., Cadule, P., Cheiney, A., Ciais, P., Hodson, E., Peylin, P., Plummer, S., Spessa, A., Saatchi, S., Yue, C., et al., 2015. Sensitivity of global terrestrial carbon cycle dynamics to variability in satellite-observed burned area. Glob. Biogeochem. Cycles 29, 207–222.
Quegan, S., Le Toan, T., Yu, J.J., Ribbes, F., Floury, N., 2000. Multitemporal ERS SAR analysis applied to forest mapping. IEEE Trans. Geosci. Remote Sens. 38, 741–753.
Ramo, R., Chuvieco, E., 2017. Developing a random forest algorithm for MODIS global burned area classification. Remote Sens. 9, 1193.
Randerson, J., Chen, Y., Werf, G., Rogers, B., Morton, D., 2012. Global burned area and biomass burning emissions from small fires. J. Geophys. Res.: Biogeosci. 117.
Reed, I.S., Yu, X., 1990. Adaptive multiple-band CFAR detection of an optical pattern with unknown spectral distribution. IEEE Trans. Acoust. Speech Signal Process. 38, 1760–1770.
Rignot, E., Despain, D., Holecz, F., 1999. The 1988 Yellowstone fires observed by imaging radars. In: Proceedings of the Joint Fire Sciences Conference and Workshop. 1.
Rodriguez-Galiano, V.F., Ghimire, B., Rogan, J., Chica-Olmo, M., Rigol-Sanchez, J.P., 2012. An assessment of the effectiveness of a random forest classifier for land-cover classification. ISPRS J. Photogramm. Remote Sens. 67, 93–104.
Roteta, E., Bastarrika, A., Padilla, M., Storm, T., Chuvieco, E., 2019. Development of a Sentinel-2 burned area algorithm: generation of a small fire database for sub-Saharan Africa. Remote Sens. Environ. 222, 1–17.
Roy, D.P., Boschetti, L., Justice, C.O., Ju, J., 2008. The collection 5 MODIS burned area product–global evaluation by comparison with the MODIS active fire product. Remote Sens. Environ. 112, 3690–3707.
Ruecker, G., Siegert, F., 2000. Burn scar mapping and fire damage assessment using ERS-2 SAR images in East Kalimantan, Indonesia. Int. Arch. Photogramm. Remote. Sens. 33, 1286–1293.
Schroeder, W., Oliva, P., Giglio, L., Csiszar, I.A., 2014. The New VIIRS 375 m active fire detection data product: algorithm description and initial assessment. Remote Sens. Environ. 143, 85–96.
Siegert, F., Hoffmann, A.A., 2000. The 1998 forest fires in East Kalimantan (Indonesia): a quantitative evaluation using high resolution, multitemporal ERS-2 SAR images and NOAA-AVHRR hotspot data. Remote Sens. Environ. 72, 64–77.
Siegert, F., Ruecker, G., 2000. Use of multitemporal ERS-2 SAR images for identification of burned scars in south-east Asian tropical rainforest. Int. J. Remote Sens. 21, 831–837.
Simon, M., Plummer, S., Fierens, F., Hoelzemann, J.J., Arino, O., 2004. Burnt area detection at global scale using ATSR-2: the GLOBSCAR products and their qualification. J. Geophys. Res.: Atmos. 109.
Small, D., 2011. Flattening gamma: radiometric terrain correction for SAR imagery. IEEE Trans. Geosci. Remote Sens. 49, 3081–3093.
Stein, D.W., Beaven, S.G., Hoff, L.E., Winter, E.M., Schaum, A.P., Stocker, A.D., 2002. Anomaly detection from hyperspectral imagery. IEEE Signal Process. Mag. 19, 58–69.
Stroppiana, D., Azar, R., Calò, F., Pepe, A., Imperatore, P., Boschetti, M., Silva, J.M., Brivio, P.A., Lanari, R., 2015b. Remote sensing of burned area: a fuzzy-based framework for joint processing of optical and microwave data. In: 2015 IEEE International Geoscience and Remote Sensing Symposium (IGARSS). IEEE, pp. 1409–1412.
Stroppiana, D., Azar, R., Calò, F., Pepe, A., Imperatore, P., Boschetti, M., Silva, J., Brivio, P.A., Lanari, R., 2015a. Integration of optical and SAR data for burned area mapping in Mediterranean Regions. Remote Sens. 7, 1320–1345.
Tanase, M.A., Santoro, M., Wegmüller, U., de la Riva, J., Pérez-Cabello, F., 2010c. Properties of X-, C-and L-band repeat-pass interferometric SAR coherence in Mediterranean pine forests affected by fires. Remote Sens. Environ. 114, 2182–2194.
Tanase, M., Kennedy, R., Aponte, C., 2015. Radar burn ratio for fire severity estimation at canopy level: an example for temperate forests. Remote Sens. Environ. 170, 14–31.
Tanase, M., de la Riva, J., Pérez-Cabello, F., 2011. Estimating burn severity at the regional level using optically based indices. Can. J. For. Res. 41, 863–872.
Tanase, M.A., Aponte, C., Mermoz, S., Bouvet, A., Le Toan, T., Heurich, M., 2018. Detection of windthrows and insect outbreaks by L-band SAR: a case study in the Bavarian Forest National Park. Remote Sens. Environ. 209, 700–711.
Tanase, M.A., Belenguer-Plomer, M.A., 2018. 03. D3 Intermediate Validation Results: SAR Pre-processing and Burned Area Detection, version 1.0. ESA Climate Change Initiative-Fire_cci.
Tanase, M.A., Perez-Cabello, F., de La Riva, J., Santoro, M., 2010a. TerraSAR-X data for burn severity evaluation in Mediterranean forests on sloped terrain. IEEE Trans. Geosci. Remote Sens. 48, 917–929.
Tanase, M., Santoro, M., de la Riva, J., Pérez-Cabello, F., 2009. Backscatter properties of multitemporal TerraSAR-X data and the effects of influencing factors on burn severity evaluation, in a Mediterranean pine forest. In: Geoscience and Remote Sensing Symposium,2009 IEEE International, IGARSS 2009. 3. IEEE, pp. III–593.
Tanase, M.A., Santoro, M., de La Riva, J., Fernando, P., Le Toan, T., et al., 2010b. Sensitivity of X-, C-, and L-band SAR backscatter to burn severity in Mediterranean pine forests. IEEE Trans. Geosci. Remote Sens. 48, 3663–3675.
Tanase, M.A., Santoro, M., Aponte, C., de la Riva, J., 2014. Polarimetric properties of burned forest areas at C-and L-band. IEEE J. Sel. Top. Appl. Earth Obs. Remote Sens. 7, 267–276.
Tansey, K., Grégoire, J.-M., Defourny, P., Leigh, R., Pekel, J.-F., van Bogaert, E., Bartholomé, E., 2008. A new, global, multi-annual (2000–2007) burnt area product at 1 km resolution. Geophys. Res. Lett. 35.
Tansey, K., Grégoire, J.-M., Stroppiana, D., Sousa, A., Silva, J., Pereira, J., Boschetti, L., Maggi, M., Brivio, P.A., Fraser, R., et al., 2004. Vegetation burning in the year 2000: global burned area estimates from SPOT VEGETATION data. J. Geophys. Res.: Atmos. 109.
Theiler, J., Perkins, S., 2006. Proposed framework for anomalous change detection. In: ICML Workshop on Machine Learning Algorithms for Surveillance and Event Detection, pp. 7–14.
Van Der Werf, G.R., Randerson, J.T., Giglio, L., Van Leeuwen, T.T., Chen, Y., Rogers, B.M., Mu, M., Van Marle, M.J., Morton, D.C., Collatz, G.J., et al., 2017. Global fire emissions estimates during 1997–2016. Earth Syst. Sci. Data 9, 697–720.
Van Wagtendonk, J.W., Root, R.R., Key, C.H., 2004. Comparison of AVIRIS and Landsat ETM+ detection capabilities for burn severity. Remote Sens. Environ. 92, 397–408.
Van Zyl, J.J., 1993. The effect of topography on radar scattering from vegetated areas. IEEE Trans. Geosci. Remote Sens. 31, 153–160.
Van Zyl, J.J., Arii, M., Kim, Y., 2011. Model-based decomposition of polarimetric SAR covariance matrices constrained for nonnegative eigenvalues. IEEE Trans. Geosci. Remote Sens. 49, 3452–3459.
Verhegghen, A., Eva, H., Ceccherini, G., Achard, F., Gond, V., Gourlet-Fleury, S., Cerutti, P.O., 2016. The potential of Sentinel satellites for burnt area mapping and monitoring in the Congo Basin forests. Remote Sens. 8, 986.
Vermote, E., Justice, C., Claverie, M., Franch, B., 2016. Preliminary analysis of the performance of the Landsat 8/OLI land surface reflectance product. Remote Sens. Environ. 185, 46–56.
Waske, B., Braun, M., 2009. Classifier ensembles for land cover mapping using multitemporal SAR imagery. ISPRS J. Photogramm. Remote Sens. 64, 450–457.
Watanabe, M., Koyama, C.N., Hayashi, M., Nagatani, I., Shimada, M., 2018. Early-stage deforestation detection in the tropics with L-band SAR. IEEE J. Sel. Top. Appl. Earth Obs. Remote Sens. 11, 2127–2133.
Van der Werf, G.R., Randerson, J.T., Giglio, L., Collatz, G., Mu, M., Kasibhatla, P.S., Morton, D.C., DeFries, R., Jin, Y. v., van Leeuwen, T.T., 2010. Global fire emissions and the contribution of deforestation, savanna, forest, agricultural, and peat fires (1997–2009). Atmos. Chem. Phys. 10, 11707–11735.
Yamaguchi, Y., Moriyama, T., Ishido, M., Yamada, H., 2005. Four-component scattering model for polarimetric SAR image decomposition. IEEE Trans. Geosci. Remote Sens. 43, 1699–1706.